Engineering Analysis with Boundary Elements 151 (2023) 406–422

Contents lists available at ScienceDirect

Engineering Analysis with Boundary Elements

journal homepage: www.elsevier.com/locate/enganabound

An inhomogeneous stabilized node-based smoothed radial point interpolation method for the multi-physics coupling responses of functionally graded magneto-electro-elastic structures

Liming Zhou [a,b], Fangting Qu [a,b], Shuhui Ren [c,d,*], Vinyas Mahesh [e,**]

[a] Key Laboratory of CNC Equipment Reliability, Ministry of Education, School of Mechanical and Aerospace Engineering, Jilin University, PR China
[b] School of Mechanical and Aerospace Engineering, Jilin University, No. 5988, Renmin Street, Changchun 130025, PR China
[c] Changchun Institute of Optics, Fine Mechanics and Physics, Chinese Academy of Sciences, Changchun 130033, PR China
[d] Key Laboratory of Space-Based Dynamic Fast Optical Imaging Technology, Chinese Academy of Sciences, Changchun 130033, PR China
[e] Royal Society Newton International Fellow, Department of Mechanical Engineering and Aeronautics, City, University of London, London EC1V 0HB, United Kingdom

ARTICLE INFO

Keywords:
Inhomogeneous stabilized node-based smoothed radial point interpolation method
Hygrothermo-magneto-electro-elastic
Multi-physics coupling
Functionally graded magneto-electro-elastic

ABSTRACT

In this paper, an inhomogeneous stabilized node-based smoothed radial point interpolation method (ISNS-RPIM) is developed for analyzing functionally graded magneto-electro-elastic (FGMEE) structures in hygrothermal environment. The change of material gradient follows the exponential function distribution. Combining with the gradient smoothing technique (GST) and the coupling constitutive relationship, and considering the hygrothermo-magneto-electro-elastic (HMEE) coupling effects of FGMEE material, the equations for ISNS-RPIM are deduced. The generalized displacement of the FGMEE structures is obtained, and the error in total energy norm, CPU time and efficiency of ISNS-RPIM, NS-RPIM and FEM are researched. Numerical examples are provided to explore the influence of the following parameters in FGMEE structures including exponential factor, hygrothermal loading and empirical constants, and demonstrate the correctness, high effectivity and insensitivity to mesh distortion of ISNS-RPIM. The present method has shown great potential in solving practical complex problems.

1. Introduction

As an inhomogeneous composite, functionally graded material (FGM) is utilized extensively in engineering applications: aerospace vehicles and electronic products, etc., the composition and properties of FGM could vary continuously along one or more specific directions [1–4]. Due to the property of reducing the stress concentration in layered composites, FGM has been widely concerned by researchers [5]. Scholars have made magneto-electro-elastic material (MEE) by combining piezomagnetic materials with piezoelectric materials. This material exhibits the unique ability in energy interconversion in multi-physic fields, which is used in a variety of energy harvesting systems, sensors, etc. [6–10]. Combining the merits of FGM and MEE material, FGMEE material is proposed to produce intelligent structures with higher performance. Recently, the multi-physics coupling analysis (thermal environment, humidity, mechanical loads) for FGMEE material is a new topic due to the complexity of the working environment of intelligent devices.

The mechanical behavior of FGMEE structures has been deeply studied [11–14], among many algorithms, the finite element method (FEM) has been broadly developed [15,16]. Bhangale and Ganesan [17,18] have calculated the natural frequency and static responses of the FGMEE plate under simply-supported boundary conditions and different exponential factors. Zenkour et al. [19–21] studied the infinite FGMEE hollow cylinder in thermal environment and calculated the radial displacement, temperature and stresses. Kattimani et al. [22,23] investigated the geometric nonlinear problems of traditional FGMEE plates using FEM. Then, they researched the porous FGMEE structures. The wave dispersion properties for nano-FGMEE beams were studied by Ebrahimi et al. [24], errors between the results and the analytical

* Corresponding author at: Changchun Institute of Optics, Fine Mechanics and Physics, Chinese Academy of Sciences, Changchun 130033, PR China.
** Corresponding author at: Royal Society Newton International Fellow, Department of Mechanical Engineering and Aeronautics, City, University of London, London, EC1V 0HB, United Kingdom.
E-mail addresses: ryougiit@gmail.com (S. Ren), vinyas.mahesh@gmail.com (V. Mahesh).

https://doi.org/10.1016/j.enganabound.2023.02.049
Received 20 October 2022; Received in revised form 1 February 2023; Accepted 25 February 2023
Available online 24 March 2023

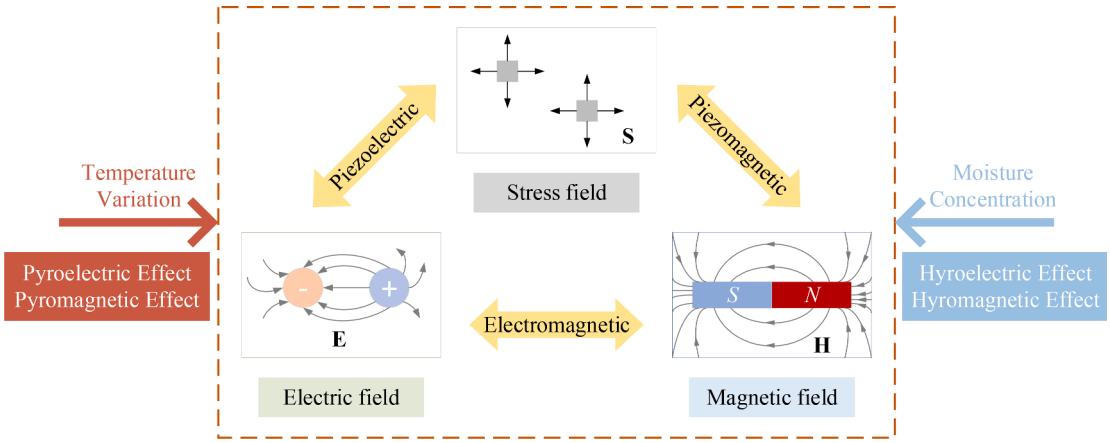

Fig. 1. Hygrothermo-magneto-electro-elastic coupling effects.

solutions were small. Mahesh et al. [25,26] researched the influence of MEE coupling effect in thermal environment on dynamic problems of FGMEE plates and carbon reinforced FGMEE structures, respectively. Recently, Vinyas [27] analyzed the dynamics of porous annular and circular FGMEE plates and obtained the factors affecting the frequency of the structures.

Studies have shown that hygrothermal environment could make smart structures more sensitive and FGMEE materials under hygrothermal loadings could produce various multi-physics coupling effects (Fig. 1) [28]. Vinyas et al. [29–31] considered the influence of thermal and hygroscopic field effects and investigated the response of MEE plates using FEM. Then, the research was extended to the skew MEE plate [32]. Dai et al. [5] obtained the responses of porous FGMEE annular plate subject to hygrothermal loadings. FGMEE nano-plate's damped frequency was calculated by Jafari et al. [33]. Saadatfar [1] considered the creep strain and analyzed the FGMEE hollow cylinders in hygrothermal environment under plane strain conditions and obtained the generalized displacement. Nguyen-Thoi et al. [34] investigated a numerical method for solving porous FGMEE plates about the free vibration and optimizing control problems.

With the constant advancement of numerical approaches, researchers devoted themselves to developing various algorithms to solve complex problems more accurately. Liu [35] proposed a series of smoothed FEMs to efficiently solve acoustic problems [36,37], multi-physics coupling problems [38], etc. Liu and Zhang [39] combined the generalized GST and weakened weak (W^2) form with RPIM to propose the smoothed RPIM (S-RPIM) [39,40], whose governing equations are without independent variable's derivative. The W^2 form without the derivative terms reduces the requirement of the approximation function [41]. In this article, the multi-physics coupling problems are solved using node-based S-RPIM (NS-RPIM) whose smoothing area is based on field nodes [42–44]. The essential boundary condition is easy to apply owing to the RPIM shape function satisfying the properties of Kronecker Delta functions. About strain energy, NS-RPIM has the advantage of upper bound property over FEM. Coordinate transformation and mapping are not required is another feature of NS-RPIM, thus NS-RPIM performs well in dealing with mesh distortion problems [45–47]. However, models constructed based on node-based smoothed numerical methods are 'overly-soft', this property could result in temporal instability in free vibration analysis or dynamic analysis [39,48]. Recently, stable node-based FEM was proposed to solve practical engineering problems including fracture analysis [49], acoustic problems [50,51], multi-physics coupling problems [48,52,53], elasticity problems [54,55], etc. Due to the stable terms, the node-based smoothed models' non-zero energy modes were eliminated.

In the previous work [52,56], stabilized NS-RPIM (SNS-RPIM) was applied to investigate the FGMEE and MEE material in the presence of temperature conditions, then we investigated the factors affecting the responses of MEE materials under hygrothermal loadings. In this work, we proposed an ISNS-RPIM to accurately study the inhomogeneous HMEE coupling effects. Considering the HMEE coupling effect, the constitutive equations were derived. The node-based smoothing domain was established by triangular cells, then the domain was closed to a circular region with equal area. Four supplementary integration points are selected to derive the stable terms. This stabilization operation does not include any uncertain parameters, which is very simple. The numerical examples demonstrated the characteristics of ISNS-RPIM including temporal stability, high accuracy and efficiency for analyzing FGMEE materials. The main influencing factors of the FGMEE structure are analyzed, including the exponential factor, temperature and moisture concentration variation, and empirical constants.

Structure of this paper: In Section 2, the basic theories of FGMEE materials are introduced. Section 3 represents ISNS-RPIM. Section 4 contains numerical examples using ISNS-RPIM. The last section contains our conclusions.

2. Basic equations of FGMEE materials

As for FGMEE materials, the coefficients are considered to vary constantly along z-direction. The expressions of the coefficients are

$$\mathbf{C}(\mathbf{x}) = \mathbf{C}^0 f(\mathbf{x}), \mathbf{e}(\mathbf{x}) = \mathbf{e}^0 f(\mathbf{x}), \mathbf{q}(\mathbf{x}) = \mathbf{q}^0 f(\mathbf{x}) \tag{1}$$

$$\boldsymbol{\varepsilon}(\mathbf{x}) = \boldsymbol{\varepsilon}^0 f(\mathbf{x}), \boldsymbol{\mu}(\mathbf{x}) = \boldsymbol{\mu}^0 f(\mathbf{x}), \mathbf{m}(\mathbf{x}) = \mathbf{m}^0 f(\mathbf{x}) \tag{2}$$

$$\boldsymbol{\beta}(\mathbf{x}) = \boldsymbol{\beta}^0 f(\mathbf{x}), \mathbf{p}(\mathbf{x}) = \mathbf{p}^0 f(\mathbf{x}), \boldsymbol{\tau}(\mathbf{x}) = \boldsymbol{\tau}^0 f(\mathbf{x}) \tag{3}$$

$$\boldsymbol{\chi}(\mathbf{x}) = \boldsymbol{\chi}^0 f(\mathbf{x}), \boldsymbol{\xi}(\mathbf{x}) = \boldsymbol{\xi}^0 f(\mathbf{x}), \boldsymbol{\gamma}(\mathbf{x}) = \boldsymbol{\gamma}^0 f(\mathbf{x}) \tag{4}$$

where C, e and q represent elastic, piezoelectric and piezomagnetic coefficient matrices, respectively. ε, μ and m represent the dielectric, magnetic permeability and magneto-electric coefficient matrices, respectively. β, χ, p, ξ, τ and γ are the vectors of thermal expansion, moisture expansion, pyroelectric, hygroelectric, pyromagnetic and hygromagnetic coefficient, respectively. z denotes the value of space coordinates in z-direction. $\mathbf{C}^0$, $\mathbf{e}^0$, $\mathbf{q}^0$, $\boldsymbol{\varepsilon}^0$, $\boldsymbol{\mu}^0$, $\mathbf{m}^0$, $\boldsymbol{\beta}^0$, $\mathbf{p}^0$, $\boldsymbol{\tau}^0$, $\boldsymbol{\chi}^0$, $\boldsymbol{\xi}^0$ and $\boldsymbol{\gamma}^0$ are the corresponding material constants for the bottom margin of the structural geometry. $f(\mathbf{x})$ denotes the exponential function, whose expression is

$$f(\mathbf{x}) = e^{\frac{nz}{w}} \tag{5}$$

where n and w denote the exponential factor and the thickness of the structure, respectively. z is the spatial coordinate.

For FGMEE structures, the constitutive equations are

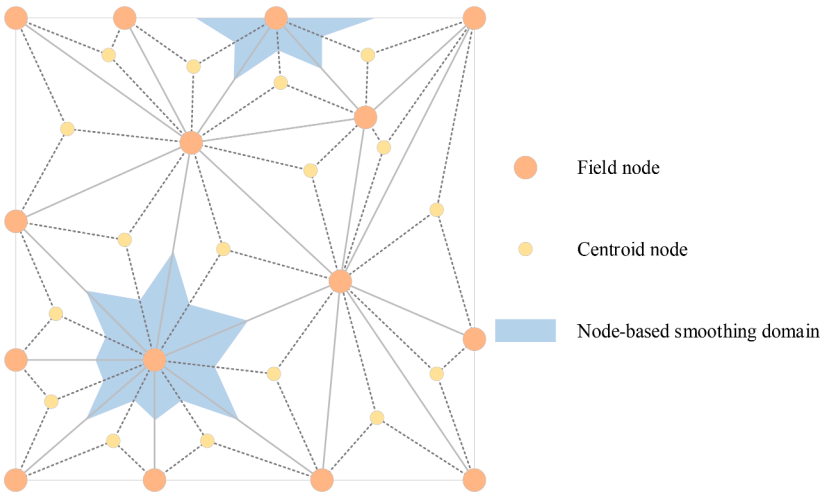

Fig. 2. Node-based smoothing domain.

$$\begin{Bmatrix} \boldsymbol{\sigma}(\mathbf{x}) \\ \mathbf{D}(\mathbf{x}) \\ \mathbf{B}(\mathbf{x}) \end{Bmatrix} = \begin{bmatrix} \mathbf{C}(\mathbf{x}) & -\mathbf{e}(\mathbf{x}) & -\mathbf{q}(\mathbf{x}) \\ \mathbf{e}^{\mathrm{T}}(\mathbf{x}) & \boldsymbol{\varepsilon}(\mathbf{x}) & \mathbf{m}(\mathbf{x}) \\ \mathbf{q}^{\mathrm{T}}(\mathbf{x}) & \mathbf{m}^{\mathrm{T}}(\mathbf{x}) & \boldsymbol{\mu}(\mathbf{x}) \end{bmatrix} \begin{Bmatrix} \mathbf{S}(\mathbf{x}) \\ \mathbf{E}(\mathbf{x}) \\ \mathbf{H}(\mathbf{x}) \end{Bmatrix} + \begin{bmatrix} -\mathbf{C}(\mathbf{x})(\boldsymbol{\beta}(\mathbf{x})\Delta T + \boldsymbol{\chi}(\mathbf{x})\Delta m) \\ \mathbf{p}(\mathbf{x})\Delta T + \boldsymbol{\xi}(\mathbf{x})\Delta m \\ \boldsymbol{\tau}(\mathbf{x})\Delta T + \boldsymbol{\gamma}(\mathbf{x})\Delta m \end{bmatrix} \tag{6}$$

where $\boldsymbol{\sigma}(\mathbf{x})$, $\mathbf{D}(\mathbf{x})$ and $\mathbf{B}(\mathbf{x})$ are the vectors of stress, electrical displacement and magnetic field intensity, respectively. $\Delta T = T - T_0$, $\Delta m = m - m_0$, T and T_0 represent the final temperature and reference temperature, m and m_0 represent the final moisture concentration and reference moisture concentration. The temperature and moisture concentration rise uniformly.

The equilibrium equations are

$$\nabla \cdot \boldsymbol{\sigma}(\mathbf{x}) = 0 \tag{7}$$

$$\nabla \cdot \mathbf{D}(\mathbf{x}) = 0 \tag{8}$$

$$\nabla \cdot \mathbf{B}(\mathbf{x}) = 0 \tag{9}$$

The geometric equations have the following formulations [57]

$$\mathbf{S}(\mathbf{x}) = \frac{1}{2}\left(\nabla \mathbf{u}(\mathbf{x}) + (\nabla \mathbf{u}(\mathbf{x}))^{\mathrm{T}}\right) \tag{10}$$

$$\mathbf{E}(\mathbf{x}) = -\nabla \boldsymbol{\Phi}(\mathbf{x}) \tag{11}$$

$$\mathbf{H}(\mathbf{x}) = -\nabla \boldsymbol{\Psi}(\mathbf{x}) \tag{12}$$

Where ∇ is the Nabla operator. $\mathbf{S}(\mathbf{x})$, u(x) are the vector of strain and displacement,$\mathbf{E}(\mathbf{x})$, $\Phi(\mathbf{x})$ are the vector of electrical field and electric potential. $\mathbf{H}(\mathbf{x})$, $\Psi(\mathbf{x})$ are the vectors of magnetic flux and magnetic potential.

3. NS-RPIM

3.1. Generalized displacement approximation using RPIM

Since the three-node triangular element is easy to be generated and has good adaptability to complex structures, it is used to discretize models in this paper [58]. To construct RPIM shape function, selecting local support nodes from different layers for interpolation is used by cell-based T2L-shceme[39].

The approximation $w(\mathbf{x})$ of generalized displacement for FGMEE material is [59]

$$w(\mathbf{x}) = \sum_{i=1}^{N_s} R_i(\mathbf{x}) a_i + \sum_{j=1}^{3} p_j(\mathbf{x}) b_j \tag{13}$$

where $R_i(\mathbf{x})$, $p_j(\mathbf{x})$denotes multi-quadrics radial basis function (MQ-RBF) and PBF [60,61], N_s is the sum of two-layer local support nodes. a_i and b_j are the coefficients related to RBF and PBF but not known, respectively.

Owing to forcing each local support node to satisfy Eq. (13), we obtain

$$\mathbf{w} = \mathbf{R}_{\mathrm{m}}\mathbf{a} + \mathbf{P}_{\mathrm{m}}\mathbf{b} \tag{14}$$

where $\mathrm{R_m}$ and $\mathrm{P_m}$ are the moment matrices.

The constrain conditions are used to guarantee the unique solution to the coefficients

$$\mathbf{P}_{\mathrm{m}}^{\mathrm{T}}\mathbf{a} = 0 \tag{15}$$

Combining Eqs. (14) and (15)

$$\begin{bmatrix} \mathbf{R}_{\mathrm{m}} & \mathbf{P}_{\mathrm{m}} \\ \mathbf{P}_{\mathrm{m}}^{\mathrm{T}} & 0 \end{bmatrix} \begin{Bmatrix} \mathbf{a} \\ \mathbf{b} \end{Bmatrix} = \begin{bmatrix} \mathbf{w} \\ 0 \end{bmatrix} \tag{16}$$

Based on Eqs. (13) and (16)

$$w(\mathbf{x}) = \overline{\mathbf{N}}(\mathbf{x}) \begin{bmatrix} \mathbf{w} \\ 0 \end{bmatrix} \tag{17}$$

where

$$\overline{\mathbf{N}}(\mathbf{x}) = \begin{bmatrix} \mathbf{R}^{\mathrm{T}}(\mathbf{x}) & \mathbf{p}^{\mathrm{T}}(\mathbf{x}) \end{bmatrix} \begin{bmatrix} \mathbf{R}_{\mathrm{m}} & \mathbf{P}_{\mathrm{m}} \\ \mathbf{P}_{\mathrm{m}}^{\mathrm{T}} & 0 \end{bmatrix}^{-1} = \begin{bmatrix} N_1(\mathbf{x}) & N_2(\mathbf{x}) & \cdots & N_{N_s+3}(\mathbf{x}) \end{bmatrix} \tag{18}$$

The RPIM shape function is $\mathbf{N}(\mathbf{x}) = \begin{bmatrix} N_1(\mathbf{x}) & N_2(\mathbf{x}) & \cdots & N_{N_s}(\mathbf{x}) \end{bmatrix}$.

3.2. Inhomogeneous node-based GST

Due to the limitation of low accuracy in dealing with multi-physics coupling problems using FEM, a new algorithm be developed to accurately analyze the responses of FGMEE structures. By linking the centroid nodes and the mid-edge points around node x_i, the node-based smoothing domain Ω_i is created (Fig. 2). Using RPIM shape functions of displacement $\mathbf{N}_i^{\mathrm{u}}(\mathbf{x})$, electric potential $\mathbf{N}_i^{\Phi}(\mathbf{x})$and magnetic potential $\mathbf{N}_i^{\Psi}(\mathbf{x})$. the displacement function $\overline{\mathbf{u}}_i(\mathbf{x})$, electric potential function $\overline{\Phi}_i(\mathbf{x})$ and magnetic potential function $\overline{\Psi}_i(\mathbf{x})$ are given as

$$\overline{\mathbf{u}}_i(\mathbf{x}) = \mathbf{N}_i^{\mathrm{u}}(\mathbf{x})\mathbf{u}_i(\mathbf{x}) \tag{19}$$

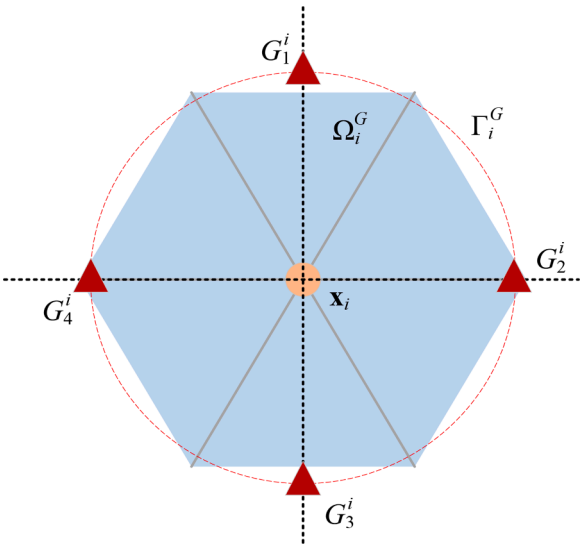

Fig. 3. The approximate domain of ISNS-RPIM.

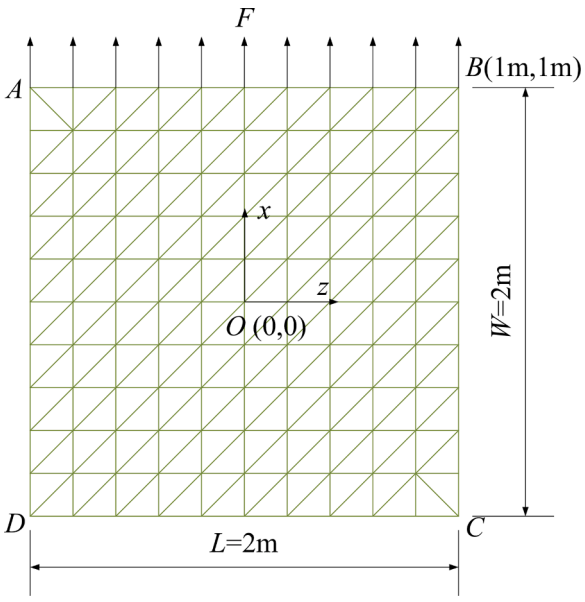

Fig. 4. Meshes and dimensions of the MEE plate.

Table 1
Material parameters of $BaTiO_3$-$CoFe_2O_4$ [25,63].

Elastic coefficient C-N/m^2					
C_{11}	C_{12}	C_{13}	C_{33}	C_{44}	C_{66}
1.66×10^{11}	0.77×10^{11}	0.78×10^{11}	1.62×10^{11}	0.43×10^{11}	0.445×10^{11}
Piezoelectric coefficient e-C/m^2			Piezomagnetic coefficient q-N/Am		
e_{31}	e_{33}	e_{15}	q_{31}	q_{33}	q_{15}
−4.4	18.6	11.6	580.3	699.7	550.0
Dielectric coefficient ε-C^2/Nm^2		Magneto-electric coefficient m-Ns/VC		Magnetic permeability μ-Ns^2/C^2	
ε_{11}	ε_{33}	m_{11}	m_{33}	μ_{11}	μ_{33}
1.12×10^{-8}	1.26×10^{-8}	5.0×10^{-12}	3.0×10^{-12}	5.0×10^{-6}	10.0×10^{-6}
Pyroelectric coefficient p-C/m^{2}K	Pyromagnetic coefficient τ- C/m^{2}K	hygroelectric coefficient ξ-Cm/kg	hygromagnetic coefficient γ-Nm^2/Akg		
p_3	τ_3	ξ	γ		
-13×10^{-5}	6×10^{-3}	0	0		
Thermal expansion coefficient β-K^{-1}		Moisture expansion coefficient χ-m^3/kg		Density ρ-kg/m^3	
$\beta_1=\beta_2$	β_3	$\chi_2=\chi_3$		ρ	
14.1×10^{-6}	7.2×10^{-6}	1.1×10^{-4}		5730	

$$\overline{\Phi}_i(\mathbf{x})=\mathbf{N}_i^{\Phi}(\mathbf{x})\mathbf{\Phi}_i(\mathbf{x}) \tag{20}$$

$$\overline{\Psi}_i(\mathbf{x})=\mathbf{N}_i^{\Psi}(\mathbf{x})\mathbf{\Psi}_i(\mathbf{x}) \tag{21}$$

The smoothed strain $\overline{\mathbf{S}}_i(\mathbf{x})$, smoothed electrical field intensity $\overline{\mathbf{E}}_i(\mathbf{x})$ and smoothed magnetic flux density $\overline{\mathbf{H}}_i(\mathbf{x})$ are given as

$$\overline{\mathbf{S}}_i(\mathbf{x})=\frac{1}{A_i}\int_{\Gamma_i}\mathbf{L}_{\mathrm{n}}^{\mathrm{u}}\overline{\mathbf{u}}_i(\mathbf{x})\mathrm{d}\Gamma=\sum_{j=1}^{N_s}\left[\overline{\mathbf{B}}_i^{\mathrm{u}}(\mathbf{x})\right]_j[\mathbf{u}_i(\mathbf{x})]_j \tag{22}$$

$$\overline{\mathbf{E}}_i(\mathbf{x})=\frac{1}{A_i}\int_{\Gamma_i}\mathbf{L}_{\mathrm{n}}^{\Phi}\overline{\Phi}_i(\mathbf{x})\mathrm{d}\Gamma=-\sum_{j=1}^{N_s}\left[\overline{\mathbf{B}}_i^{\Phi}(\mathbf{x})\right]_j[\mathbf{\Phi}_i(\mathbf{x})]_j \tag{23}$$

$$\overline{\mathbf{H}}_i(\mathbf{x})=\frac{1}{A_i}\int_{\Gamma_i}\mathbf{L}_{\mathrm{n}}^{\Psi}\overline{\Psi}_i(\mathbf{x})\mathrm{d}\Gamma=-\sum_{j=1}^{N_s}\left[\overline{\mathbf{B}}_i^{\Psi}(\mathbf{x})\right]_j[\mathbf{\Psi}_i(\mathbf{x})]_j \tag{24}$$

where A_i denotes the area of Ω_i and Γ_i denotes the boundary of Ω_i. $\mathbf{L}_{\mathrm{n}}^{\mathrm{u}}$, $\mathbf{L}_{\mathrm{n}}^{\Phi}$ and $\mathbf{L}_{\mathrm{n}}^{\Psi}$ are the unit normal vector matrices

$$\mathbf{L}_{\mathrm{n}}^{\mathrm{u}}=\begin{bmatrix}n_x & 0 & n_z\\ 0 & n_z & n_x\end{bmatrix}^{\mathrm{T}},\mathbf{L}_{\mathrm{n}}^{\Phi}=\mathbf{L}_{\mathrm{n}}^{\Psi}=[n_x \quad n_z]^{\mathrm{T}} \tag{25}$$

$[\overline{\mathbf{B}}_i^{\mathrm{u}}(\mathbf{x})]_j$, $[\overline{\mathbf{B}}_i^{\Phi}(\mathbf{x})]_j$ and $[\overline{\mathbf{B}}_i^{\Psi}(\mathbf{x})]_j$ could be expressed as

$$\left[\overline{\mathbf{B}}_i^{\mathrm{u}}(\mathbf{x})\right]_j=\begin{bmatrix}\left(\overline{b}_{jx}^{\mathrm{u}}(\mathbf{x})\right)_i & 0 & \left(\overline{b}_{jz}^{\mathrm{u}}(\mathbf{x})\right)_i\\ 0 & \left(\overline{b}_{jz}^{\mathrm{u}}(\mathbf{x})\right)_i & \left(\overline{b}_{jx}^{\mathrm{u}}(\mathbf{x})\right)_i\end{bmatrix}^{\mathrm{T}} \tag{26}$$

$$\left[\overline{\mathbf{B}}_i^{\Phi}(\mathbf{x})\right]_j=\begin{bmatrix}\left(\overline{b}_{jx}^{\Phi}(\mathbf{x})\right)_i & \left(\overline{b}_{jz}^{\Phi}(\mathbf{x})\right)_i\end{bmatrix}^{\mathrm{T}},\left[\overline{\mathbf{B}}_i^{\Psi}(\mathbf{x})\right]_j=\begin{bmatrix}\left(\overline{b}_{jx}^{\Psi}(\mathbf{x})\right)_i & \left(\overline{b}_{jz}^{\Psi}(\mathbf{x})\right)_i\end{bmatrix}^{\mathrm{T}} \tag{27}$$

Substituting $\overline{\mathbf{S}}_i(\mathbf{x})$, $\overline{\mathbf{E}}_i(\mathbf{x})$ and $\overline{\mathbf{H}}_i(\mathbf{x})$ defined in Eqs. (7)–(9) by Eqs. (22)–(24), the stiffness matrices for FGMEE structures with N nodes can be computed as

$$\mathbf{K}_{\mathrm{uu}}=\sum_{i=1}^{N}A_i\left[\overline{\mathbf{B}}_i^{\mathrm{u}}(\mathbf{x})\right]^{\mathrm{T}}\mathbf{C}(\mathbf{x})\left[\overline{\mathbf{B}}_i^{\mathrm{u}}(\mathbf{x})\right],\mathbf{K}_{\Phi\Phi}=\sum_{i=1}^{N}A_i\left[\overline{\mathbf{B}}_i^{\Phi}(\mathbf{x})\right]^{\mathrm{T}}\boldsymbol{\varepsilon}(\mathbf{x})\left[\overline{\mathbf{B}}_i^{\Phi}(\mathbf{x})\right] \tag{28}$$

$$\mathbf{K}_{\Psi\Psi}=\sum_{i=1}^{N}A_i\left[\overline{\mathbf{B}}_i^{\Psi}(\mathbf{x})\right]^{\mathrm{T}}\boldsymbol{\mu}(\mathbf{x})\left[\overline{\mathbf{B}}_i^{\Psi}(\mathbf{x})\right],\mathbf{K}_{\mathrm{u}\Phi}=\sum_{i=1}^{N}A_i\left[\overline{\mathbf{B}}_i^{\mathrm{u}}(\mathbf{x})\right]^{\mathrm{T}}\mathbf{e}(\mathbf{x})\left[\overline{\mathbf{B}}_i^{\Phi}(\mathbf{x})\right] \tag{29}$$

$$\mathbf{K}_{\mathrm{u}\Psi}=\sum_{i=1}^{N}A_i\left[\overline{\mathbf{B}}_i^{\mathrm{u}}(\mathbf{x})\right]^{\mathrm{T}}\mathbf{q}(\mathbf{x})\left[\overline{\mathbf{B}}_i^{\Psi}(\mathbf{x})\right],\mathbf{K}_{\Phi\Psi}=\sum_{i=1}^{N}A_i\left[\overline{\mathbf{B}}_i^{\Phi}(\mathbf{x})\right]^{\mathrm{T}}\mathbf{m}(\mathbf{x})\left[\overline{\mathbf{B}}_i^{\Psi}(\mathbf{x})\right] \tag{30}$$

3.3. ISNS-RPIM

To guarantee stability and accuracy in solving dynamic problems, stable terms need to be introduced into NS-RPIM [42,62]. The stable terms are constructed based on Ω_i (Fig. 3). Ω_i defined as approximate domain is closed to a circular region Ω_i^G whose area is the same as A_i. Then Ω_i^G is subdivided to four sub-regions. The radius of the approximate domain is

$$l_{\mathrm{c}}=\sqrt{A_i/\pi} \tag{31}$$

Table 2
Generalized displacement of point *B*.

	u_x (10^{-10} m)	u_z (10^{-9} m)	Φ (V)	Ψ (10^{-2}A)
ISNS-RPIM	−6.333170612063460	1.1366757464314900	1.8990980642225400	4.27812431865876
Analytical Solution	−6.3332000	1.1366760	1.8991000	4.278120

Table 3
The efficiency of EFGM, FEM and ISNS-RPIM [64].

Method	CPU time/s	Energy error (%)	*EC*
EFGM	6.004	6.609×10^{-5}	2.52×10^{3}
FEM	1.746	3.047×10^{-4}	1.88×10^{3}
ISNS-RPIM	16.386	7.223×10^{-6}	8.45×10^{3}

The gradient of u, Φ and Ψ at node $\mathbf{x}_i$ are

$$\nabla\mathbf{u} = \nabla\mathbf{u}_i + \frac{\partial(\nabla\mathbf{u})}{\partial x}(x-x_i) + \frac{\partial(\nabla\mathbf{u})}{\partial z}(z-z_i) \tag{32}$$

$$\nabla\boldsymbol{\Phi} = \nabla\boldsymbol{\Phi}_i + \frac{\partial(\nabla\boldsymbol{\Phi})}{\partial x}(x-x_i) + \frac{\partial(\nabla\boldsymbol{\Phi})}{\partial z}(z-z_i) \tag{33}$$

$$\nabla\boldsymbol{\Psi} = \nabla\boldsymbol{\Psi}_i + \frac{\partial(\nabla\boldsymbol{\Psi})}{\partial x}(x-x_i) + \frac{\partial(\nabla\boldsymbol{\Psi})}{\partial z}(z-z_i) \tag{34}$$

The gradient items of complementary integration points G_k^i (k=1, 2, 3, 4) are

$$(\nabla\mathbf{u})_{i1} = \nabla\mathbf{u}_i + l_c\cdot\partial(\nabla\mathbf{u})/\partial x, (\nabla\mathbf{u})_{i2} = \nabla\mathbf{u}_i + l_c\cdot\partial(\nabla\mathbf{u})/\partial z \tag{35}$$

$$(\nabla\mathbf{u})_{i3} = \nabla\mathbf{u}_i - l_c\cdot\partial(\nabla\mathbf{u})/\partial x, (\nabla\mathbf{u})_{i4} = \nabla\mathbf{u}_i - l_c\cdot\partial(\nabla\mathbf{u})/\partial z \tag{36}$$

$$(\nabla\boldsymbol{\Phi})_{i1} = \nabla\boldsymbol{\Phi}_i + l_c\cdot\partial(\nabla\boldsymbol{\Phi})/\partial x, (\nabla\boldsymbol{\Phi})_{i2} = \nabla\boldsymbol{\Phi}_i + l_c\cdot\partial(\nabla\boldsymbol{\Phi})/\partial z \tag{37}$$

$$(\nabla\boldsymbol{\Phi})_{i3} = \nabla\boldsymbol{\Phi}_i - l_c\cdot\partial(\nabla\boldsymbol{\Phi})/\partial x, (\nabla\boldsymbol{\Phi})_{i4} = \nabla\boldsymbol{\Phi}_i - l_c\cdot\partial(\nabla\boldsymbol{\Phi})/\partial z \tag{38}$$

$$(\nabla\boldsymbol{\Psi})_{i1} = \nabla\boldsymbol{\Psi}_i + l_c\cdot\partial(\nabla\boldsymbol{\Psi})/\partial x, (\nabla\boldsymbol{\Psi})_{i2} = \nabla\boldsymbol{\Psi}_i + l_c\cdot\partial(\nabla\boldsymbol{\Psi})/\partial z \tag{39}$$

$$(\nabla\boldsymbol{\Psi})_{i3} = \nabla\boldsymbol{\Psi}_i - l_c\cdot\partial(\nabla\boldsymbol{\Psi})/\partial x, (\nabla\boldsymbol{\Psi})_{i4} = \nabla\boldsymbol{\Psi}_i - l_c\cdot\partial(\nabla\boldsymbol{\Psi})/\partial z \tag{40}$$

The modified stiffness matrices are obtained by Eqs. (35)–(40) as follow

$$\overline{\mathbf{K}}_{\mathrm{uu}} = \mathbf{K}_{\mathrm{uu}} + \mathbf{K}^*_{\mathrm{uu}}, \overline{\mathbf{K}}_{\Phi\Phi} = \mathbf{K}_{\Phi\Phi} + \mathbf{K}^*_{\Phi\Phi}, \overline{\mathbf{K}}_{\Psi\Psi} = \mathbf{K}_{\Psi\Psi} + \mathbf{K}^*_{\Psi\Psi}, \tag{41}$$

$$\overline{\mathbf{K}}_{\mathrm{u}\Phi} = \mathbf{K}_{\mathrm{u}\Phi} + \mathbf{K}^*_{\mathrm{u}\Phi}, \overline{\mathbf{K}}_{\mathrm{u}\Psi} = \mathbf{K}_{\mathrm{u}\Psi} + \mathbf{K}^*_{\mathrm{u}\Psi}, \overline{\mathbf{K}}_{\Phi\Psi} = \mathbf{K}_{\Phi\Psi} + \mathbf{K}^*_{\Phi\Psi}, \tag{42}$$

$$\mathbf{K}^*_{\mathrm{uu}} = \sum_{i=1}^{N}\frac{A_i}{2}\left[\left[\overline{\mathbf{B}}_i^{\mathrm{u}}\right]_x^{\mathrm{T}}\mathbf{C}(\mathbf{x})\left[\overline{\mathbf{B}}_i^{\mathrm{u}}\right]_x + \left[\overline{\mathbf{B}}_i^{\mathrm{u}}\right]_z^{\mathrm{T}}\mathbf{C}(\mathbf{x})\left[\overline{\mathbf{B}}_i^{\mathrm{u}}\right]_z\right] \tag{43}$$

$$\mathbf{K}^*_{\mathrm{u}\Phi} = \sum_{i=1}^{N}\frac{A_i}{2}\left[\left[\overline{\mathbf{B}}_i^{\mathrm{u}}\right]_x^{\mathrm{T}}\mathbf{e}(\mathbf{x})\left[\overline{\mathbf{B}}_i^{\Phi}\right]_x + \left[\overline{\mathbf{B}}_i^{\mathrm{u}}\right]_z^{\mathrm{T}}\mathbf{e}(\mathbf{x})\left[\overline{\mathbf{B}}_i^{\Phi}\right]_z\right] \tag{44}$$

$$\mathbf{K}^*_{\mathrm{u}\Psi} = \sum_{i=1}^{N}\frac{A_i}{2}\left[\left[\overline{\mathbf{B}}_i^{\mathrm{u}}\right]_x^{\mathrm{T}}\mathbf{q}(\mathbf{x})\left[\overline{\mathbf{B}}_i^{\Psi}\right]_x + \left[\overline{\mathbf{B}}_i^{\mathrm{u}}\right]_z^{\mathrm{T}}\mathbf{q}(\mathbf{x})\left[\overline{\mathbf{B}}_i^{\Psi}\right]_z\right] \tag{45}$$

$$\mathbf{K}^*_{\Phi\Phi} = \sum_{i=1}^{N}\frac{A_i}{2}\left[\left[\overline{\mathbf{B}}_i^{\Phi}\right]_x^{\mathrm{T}}\boldsymbol{\varepsilon}(\mathbf{x})\left[\overline{\mathbf{B}}_i^{\Phi}\right]_x + \left[\overline{\mathbf{B}}_i^{\Phi}\right]_z^{\mathrm{T}}\boldsymbol{\varepsilon}(\mathbf{x})\left[\overline{\mathbf{B}}_i^{\Phi}\right]_z\right] \tag{46}$$

$$\mathbf{K}^*_{\Psi\Psi} = \sum_{i=1}^{N}\frac{A_i}{2}\left[\left[\overline{\mathbf{B}}_i^{\Psi}\right]_x^{\mathrm{T}}\boldsymbol{\mu}(\mathbf{x})\left[\overline{\mathbf{B}}_i^{\Psi}\right]_x + \left[\overline{\mathbf{B}}_i^{\Psi}\right]_z^{\mathrm{T}}\boldsymbol{\mu}(\mathbf{x})\left[\overline{\mathbf{B}}_i^{\Psi}\right]_z\right] \tag{47}$$

$$\mathbf{K}^*_{\Phi\Psi} = \sum_{i=1}^{N}\frac{A_i}{2}\left[\left[\overline{\mathbf{B}}_i^{\Phi}\right]_x^{\mathrm{T}}\mathbf{m}(\mathbf{x})\left[\overline{\mathbf{B}}_i^{\Psi}\right]_x + \left[\overline{\mathbf{B}}_i^{\Phi}\right]_z^{\mathrm{T}}\mathbf{m}(\mathbf{x})\left[\overline{\mathbf{B}}_i^{\Psi}\right]_z\right] \tag{48}$$

The discretized system equations are

$$[\overline{\mathbf{K}}_{\mathrm{uu}}]\{\mathbf{u}\} + [\overline{\mathbf{K}}_{\mathrm{u}\Phi}]\{\boldsymbol{\Phi}\} + [\overline{\mathbf{K}}_{\mathrm{u}\Psi}]\{\boldsymbol{\Psi}\} = \{\mathbf{F}_{\mathrm{u}}\} + \{\mathbf{F}_{\mathrm{H}}\} + \{\mathbf{F}_{\mathrm{T}}\} \tag{49}$$

$$[\overline{\mathbf{K}}_{\Phi\mathrm{u}}]\{\mathbf{u}\} - [\overline{\mathbf{K}}_{\Phi\Phi}]\{\boldsymbol{\Phi}\} - [\overline{\mathbf{K}}_{\Phi\Psi}]\{\boldsymbol{\Psi}\} = -\{\mathbf{F}_{\mathrm{he}}\} - \{\mathbf{F}_{\mathrm{pe}}\} \tag{50}$$

$$[\overline{\mathbf{K}}_{\Psi\mathrm{u}}]\{\mathbf{u}\} - [\overline{\mathbf{K}}_{\Psi\Phi}]\{\boldsymbol{\Phi}\} - [\overline{\mathbf{K}}_{\Psi\Psi}]\{\boldsymbol{\Psi}\} = -\{\mathbf{F}_{\mathrm{hm}}\} - \{\mathbf{F}_{\mathrm{pm}}\} \tag{51}$$

where $\{\mathbf{F}_{\mathrm{u}}\}$, $\{\mathbf{F}_{\mathrm{H}}\}$ and $\{\mathbf{F}_{\mathrm{T}}\}$ are the load vector of mechanical, hygroscopic and thermal, respectively. $\{\mathbf{F}_{\mathrm{he}}\}$, $\{\mathbf{F}_{\mathrm{pe}}\}$, $\{\mathbf{F}_{\mathrm{hm}}\}$ and $\{\mathbf{F}_{\mathrm{pm}}\}$ denote load vectors of hygroelectric, pyroelectric, hygromagnetic, pyromagnetic, respectively. The expressions are

$$\{\mathbf{F}_{\mathrm{T}}\} = \sum_{i=1}^{N}A_i\left[\overline{\mathbf{B}}_i^{\mathrm{u}}(\mathbf{x})\right]^{\mathrm{T}}\mathbf{C}(\mathbf{x})\boldsymbol{\beta}(\mathbf{x})\Delta T, \{\mathbf{F}_{\mathrm{H}}\} = \sum_{i=1}^{N}A_i\left[\overline{\mathbf{B}}_i^{\mathrm{u}}(\mathbf{x})\right]^{\mathrm{T}}\mathbf{C}(\mathbf{x})\boldsymbol{\chi}(\mathbf{x})\Delta m \tag{52}$$

$$\{\mathbf{F}_{\mathrm{pe}}\} = \sum_{i=1}^{N}A_i\left[\overline{\mathbf{B}}_i^{\Phi}(\mathbf{x})\right]^{\mathrm{T}}\mathbf{p}(\mathbf{x})\Delta T, \{\mathbf{F}_{\mathrm{pm}}\} = \sum_{i=1}^{N}A_i\left[\overline{\mathbf{B}}_i^{\Psi}(\mathbf{x})\right]^{\mathrm{T}}\boldsymbol{\tau}(\mathbf{x})\Delta T \tag{53}$$

$$\{\mathbf{F}_{\mathrm{he}}\} = \sum_{i=1}^{N}A_i\left[\overline{\mathbf{B}}_i^{\Phi}(\mathbf{x})\right]^{\mathrm{T}}\boldsymbol{\xi}(\mathbf{x})\Delta m, \{\mathbf{F}_{\mathrm{hm}}\} = \sum_{i=1}^{N}A_i\left[\overline{\mathbf{B}}_i^{\Psi}(\mathbf{x})\right]^{\mathrm{T}}\boldsymbol{\gamma}(\mathbf{x})\Delta m \tag{54}$$

For free vibration problems, the right sides of Eqs. (49) to (51) are zero, and Eq. (49) is rewritten as

$$[\mathbf{M}]\{\ddot{\mathbf{u}}\} + [\overline{\mathbf{K}}_{\mathrm{uu}}]\{\mathbf{u}\} + [\overline{\mathbf{K}}_{\mathrm{u}\Phi}]\{\boldsymbol{\Phi}\} + [\overline{\mathbf{K}}_{\mathrm{u}\Psi}]\{\boldsymbol{\Psi}\} = 0 \tag{55}$$

where $\ddot{\mathbf{u}}$ is the acceleration vector, M is the mass matrix. whose expressions are

$$\mathbf{M} = \sum_{N_e}[diag\{m_1 \quad m_1 \quad m_2 \quad m_2 \quad m_3 \quad m_3\}] \tag{56}$$

where N_e is the count of elements in the model.

Using Eqs. (49)–(51) and the condensation method [28], the equivalent stiffness matrix $[\mathbf{K}_{eq}]$, equivalent load vector $\{\mathbf{F}_{eq}\}$ and mass matrix $[\mathbf{M}]$ satisfy the following equation

$$[\mathbf{K}_{eq}]\{\mathbf{u}\} = \{\mathbf{F}_{eq}\} \tag{57}$$

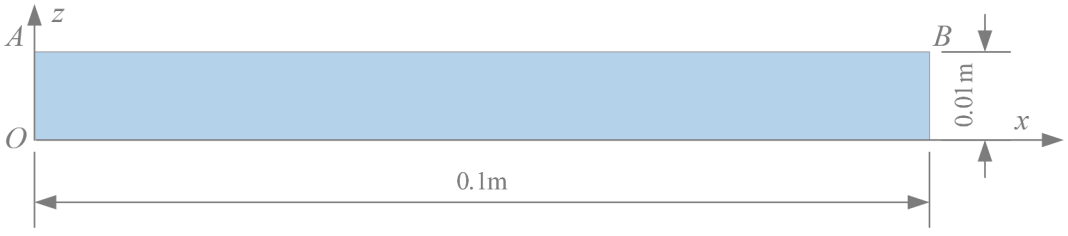

Fig. 5. FGMEE clamped-clamped beam.

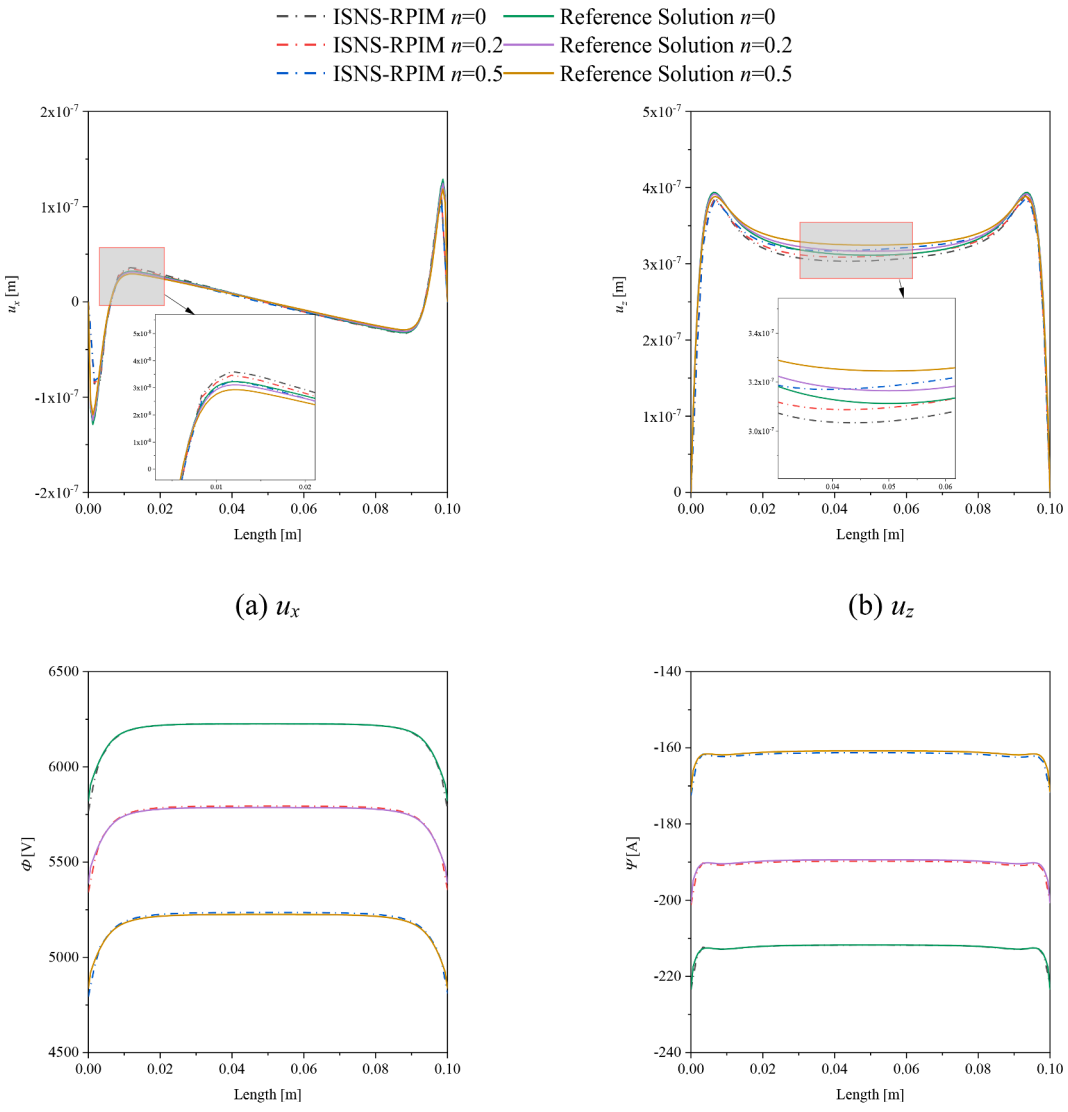

Fig. 6. The generalized displacement on edge *AB*.

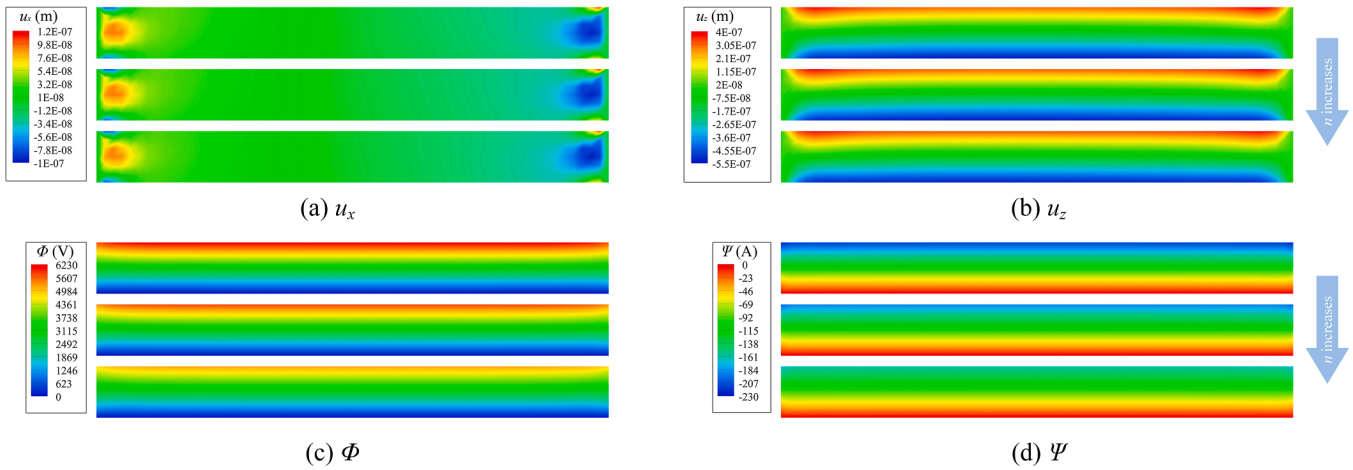

Fig. 7. FGMEE clamped-clamped beam contours.

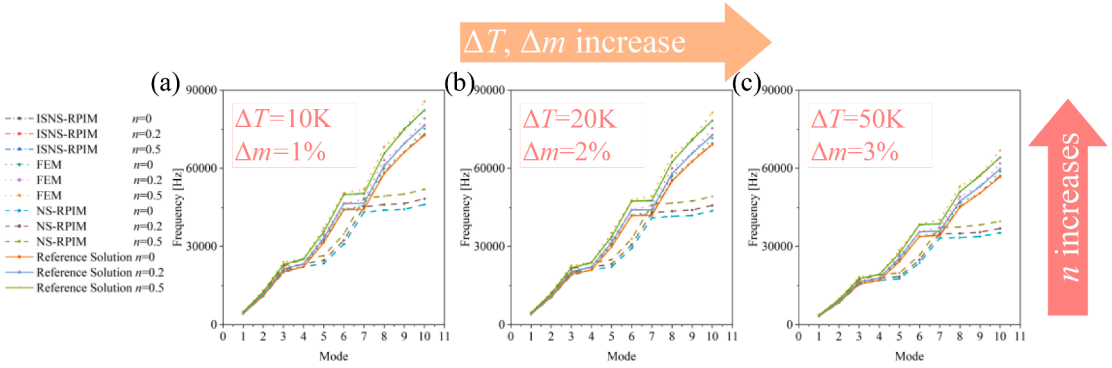

Fig. 8. Natural frequency of the FGMEE clamped-clamped beam with different hygrothermal loading. (a) $\Delta T = 10$ K, $\Delta m = 1\%$, (b) $\Delta T = 20$ K, $\Delta m = 2\%$, (c) $\Delta T = 50$ K, $\Delta m = 3\%$.

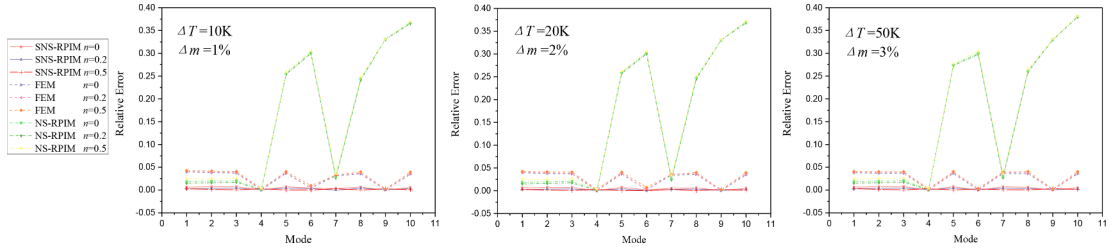

Fig. 9. Relative error of the FGMEE clamped-clamped beam with different n.

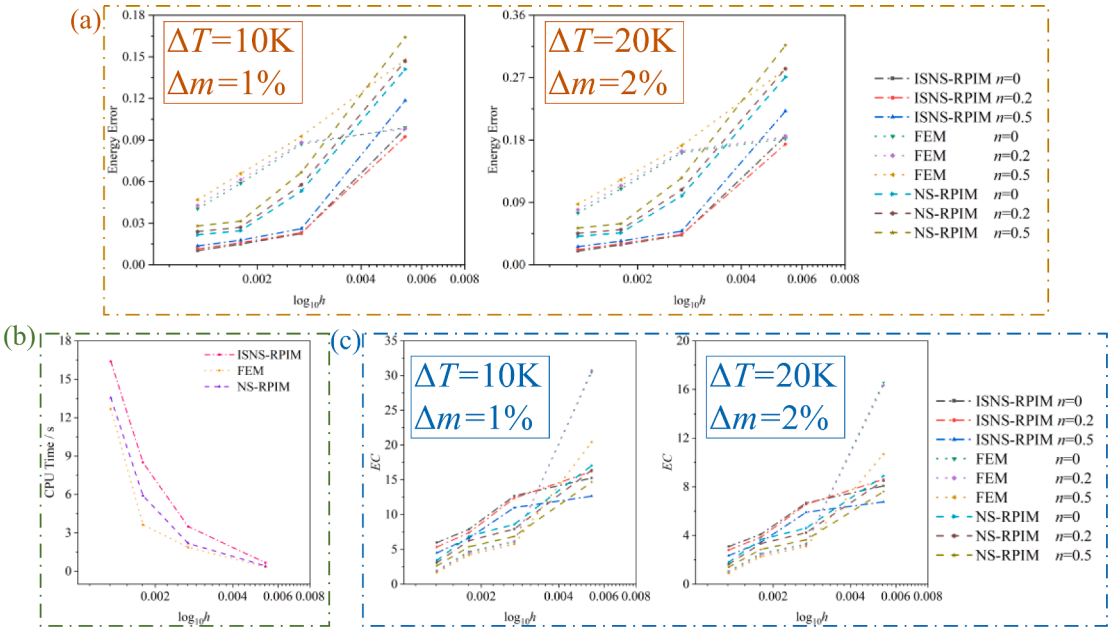

Fig. 10. (a) Energy error with different n (n=0, 0.2, 0.5) (b) CPU times (c) Efficiency with different n (n=0, 0.2, 0.5).

$$\left[\mathbf{K}_{\mathrm{eq}}\right]\{\mathbf{u}\} + [\mathbf{M}]\{\ddot{\mathbf{u}}\} = 0, \text{for free vibration problems} \tag{58}$$

The expression of Φ and Ψ and the condensation technique are written as

$$\{\boldsymbol{\Phi}\} = -[\mathbf{K}_{\mathrm{II}}]^{-1}\left\{\mathbf{F}_{\Phi\_\mathrm{sol}}\right\} + [\mathbf{K}_{\mathrm{II}}]^{-1}[\mathbf{K}_{\mathrm{I}}]\{\mathbf{u}\} \tag{59}$$

$$[\mathbf{K}_{\mathrm{I}}] = [\overline{\mathbf{K}}_{\Phi\mathrm{u}}] - [\overline{\mathbf{K}}_{\Psi\Phi}][\overline{\mathbf{K}}_{\Psi\Psi}]^{-1}[\overline{\mathbf{K}}_{\Psi\mathrm{u}}] \tag{60}$$

$$[\mathbf{K}_{\mathrm{II}}] = [\overline{\mathbf{K}}_{\Phi\Phi}] - [\overline{\mathbf{K}}_{\Psi\Phi}][\overline{\mathbf{K}}_{\Psi\Psi}]^{-1}[\overline{\mathbf{K}}_{\Phi\Psi}] \tag{61}$$

$$\{\boldsymbol{\Psi}\} = [\overline{\mathbf{K}}_{\Psi\Psi}]^{-1}[\overline{\mathbf{K}}_{\mathrm{u}\Psi}]^{\mathrm{T}}\{\mathbf{u}\} - [\overline{\mathbf{K}}_{\Psi\Psi}]^{-1}[\overline{\mathbf{K}}_{\Phi\Psi}]^{\mathrm{T}}\{\boldsymbol{\Phi}\} - [\overline{\mathbf{K}}_{\Psi\Psi}]^{-1}\left[\left\{\mathbf{F}_{\mathrm{pm}}\right\} + \left\{\mathbf{F}_{\mathrm{hm}}\right\}\right] \tag{62}$$

$$[\mathbf{K}_{\mathrm{III}}] = [\mathbf{K}_{\mathrm{II}}]^{-1}[\mathbf{K}_{\mathrm{I}}] \tag{63}$$

$$[\mathbf{K}_{\mathrm{IV}}] = [\mathbf{K}_{\mathrm{II}}]^{-1}[\overline{\mathbf{K}}_{\Psi\Phi}][\overline{\mathbf{K}}_{\Psi\Psi}] \tag{64}$$

$$[\mathbf{K}_{\mathrm{V}}] = [\overline{\mathbf{K}}_{\mathrm{uu}}] + [\overline{\mathbf{K}}_{\mathrm{u}\Psi}][\overline{\mathbf{K}}_{\Psi\Psi}]^{-1}[\overline{\mathbf{K}}_{\Psi\mathrm{u}}] \tag{65}$$

$$[\mathbf{K}_{\mathrm{VI}}] = [\overline{\mathbf{K}}_{\mathrm{u}\Phi}] - [\overline{\mathbf{K}}_{\mathrm{u}\Psi}][\overline{\mathbf{K}}_{\Psi\Psi}]^{-1}[\overline{\mathbf{K}}_{\Phi\Psi}] \tag{66}$$

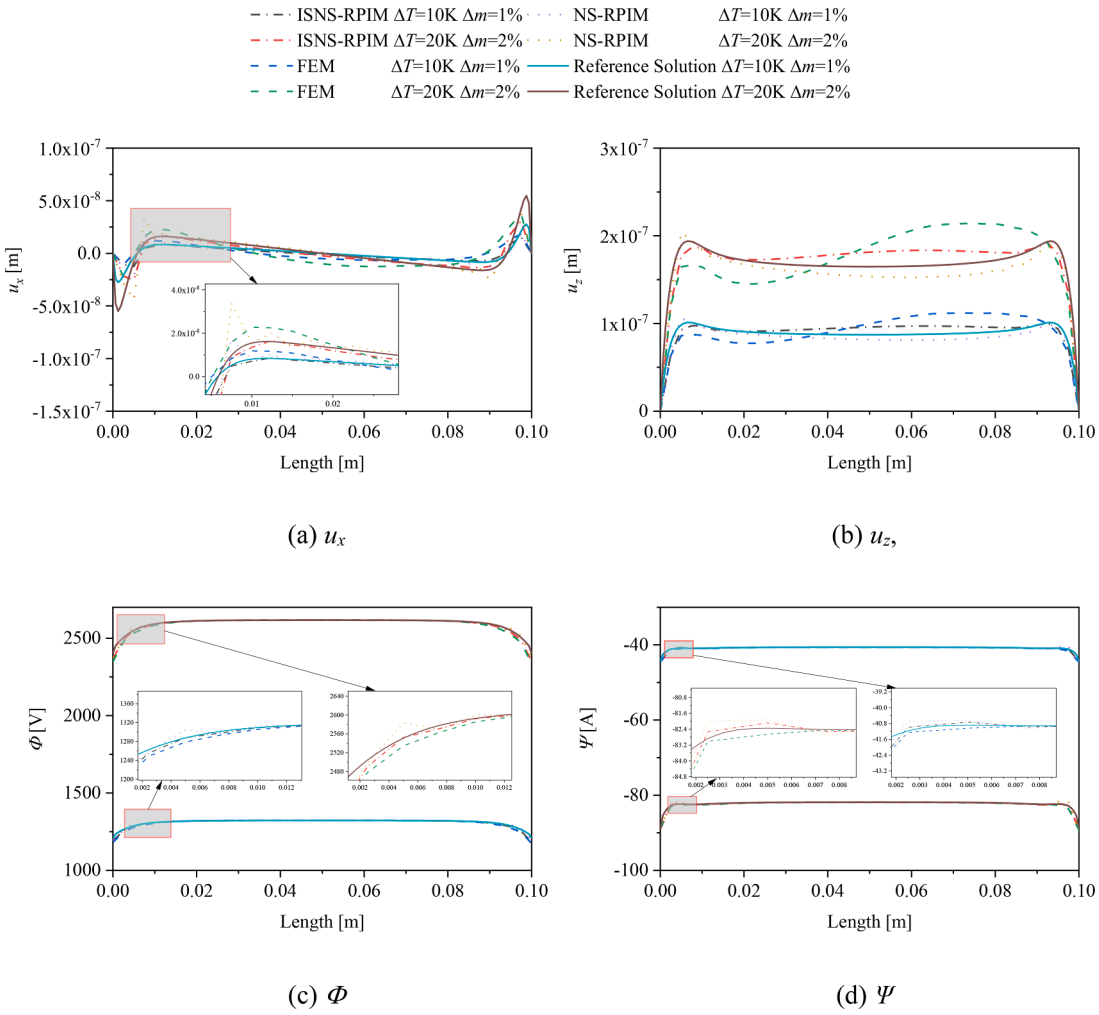

Fig. 11. The generalized displacement on edge *AB* (using distorted mesh).

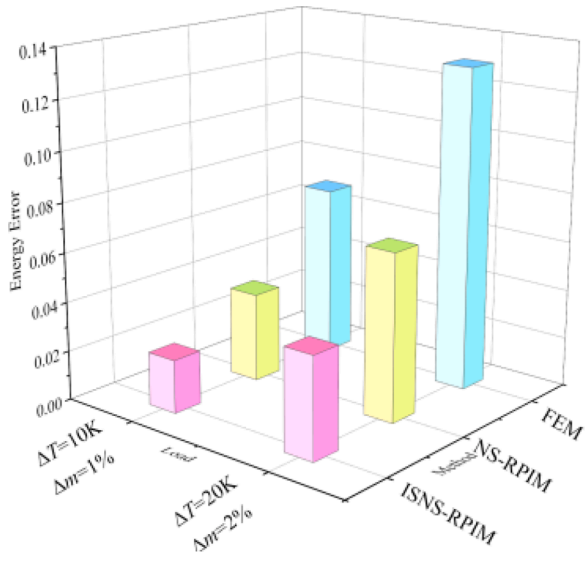

Fig. 12. The energy error using distorted mesh.

$$[\mathbf{K}_{\mathrm{VII}}] = [\mathbf{K}_{\mathrm{V}}] + [\mathbf{K}_{\mathrm{VI}}][\mathbf{K}_{\mathrm{III}}] \tag{67}$$

$$[\mathbf{K}_{\mathrm{VIII}}] = [\mathbf{K}_{\mathrm{eq}}] = [\mathbf{K}_{\mathrm{VI}}][\mathbf{K}_{\mathrm{II}}]^{-1} \tag{68}$$

$$[\mathbf{K}_{\mathrm{IX}}] = [\overline{\mathbf{K}}_{\mathrm{u}\Psi}][\overline{\mathbf{K}}_{\Psi\Psi}]^{-1} - [\overline{\mathbf{K}}_{\mathrm{VI}}][\overline{\mathbf{K}}_{\mathrm{IV}}] \tag{69}$$

$$[\mathbf{F}_{\mathbf{eq}}] = [\mathbf{K}_{\mathrm{IX}}]\left[\{\mathbf{F}_{\mathrm{pm}}\} + \{\mathbf{F}_{\mathrm{hm}}\}\right] + [\mathbf{K}_{\mathrm{VIII}}]\left[\{\mathbf{F}_{\mathrm{pe}}\} + \{\mathbf{F}_{\mathrm{he}}\}\right] + \{\mathbf{F}_{\mathrm{u}}\} + \{\mathbf{F}_{\mathrm{T}}\} + \{\mathbf{F}_{\mathrm{H}}\} \tag{70}$$

$$\{\mathbf{F}_{\Phi\_\mathrm{sol}}\} = \left[\{\mathbf{F}_{\mathrm{pe}}\} + \{\mathbf{F}_{\mathrm{he}}\}\right] - [\overline{\mathbf{K}}_{\Psi\Phi}]^{\mathrm{T}}[\overline{\mathbf{K}}_{\Psi\Psi}]^{-1}\left[\{\mathbf{F}_{\mathrm{pm}}\} + \{\mathbf{F}_{\mathrm{hm}}\}\right] \tag{71}$$

4. Numerical Examples

FGMEE structures subject to mechanical and hygrothermal loadings are studied using ISNS-RPIM in this section. Because of the small variation in temperature and moisture concentration, the following coefficients β, p, τ, χ, ξ and γ are neglected. First, the correctness of ISNS-RPIM is validated compared to the analytical solution. Then, several examples illustrate the advantages of the algorithm. Finally, the effects of exponential factor, hygrothermal loadings and empirical constants on the responses of FGMEE structures are analyzed.

The values of ξ and γ are zero. Table 1 gives the material constants of $BaTiO_3$-$CoFe_2O_4$. The influence of the empirical constants related to temperature and moisture dependency (α^*, β^*) is considered. The

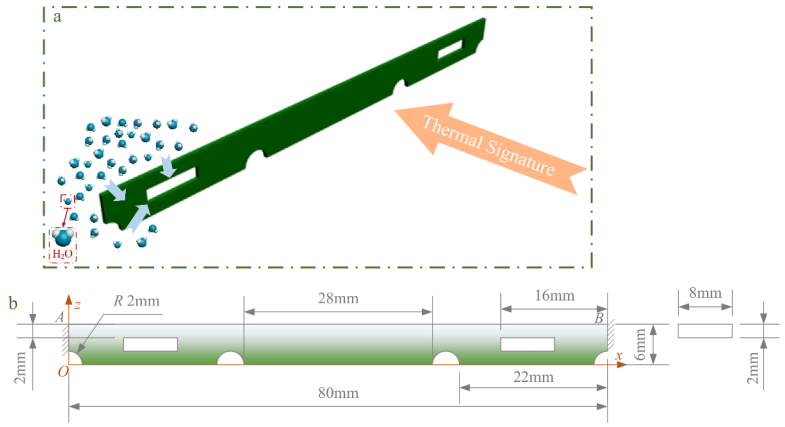

Fig. 13. (a) FGMEE energy harvester (b) Dimensions of the FGMEE energy harvester.

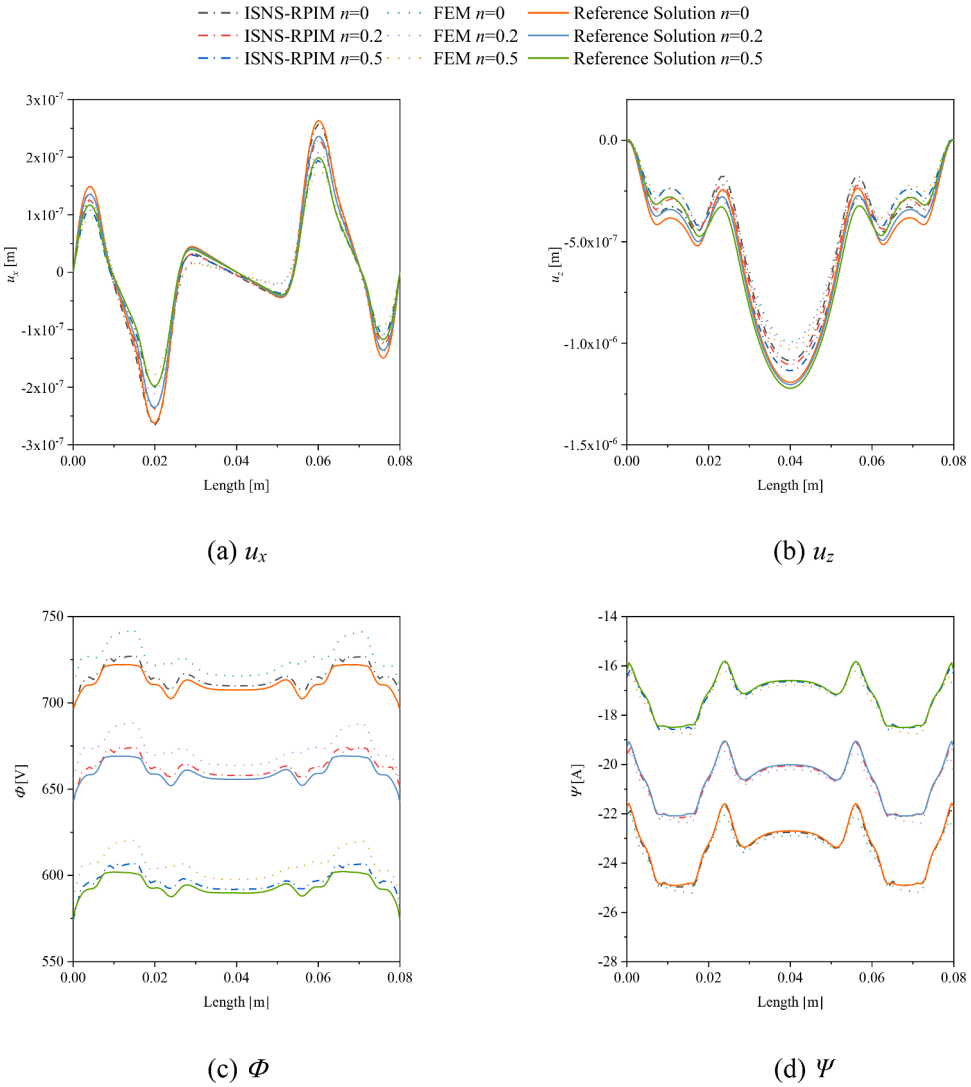

Fig. 14. The generalized displacement on edge AB ($\Delta T = 10$ K, $\Delta m = 1\%$).

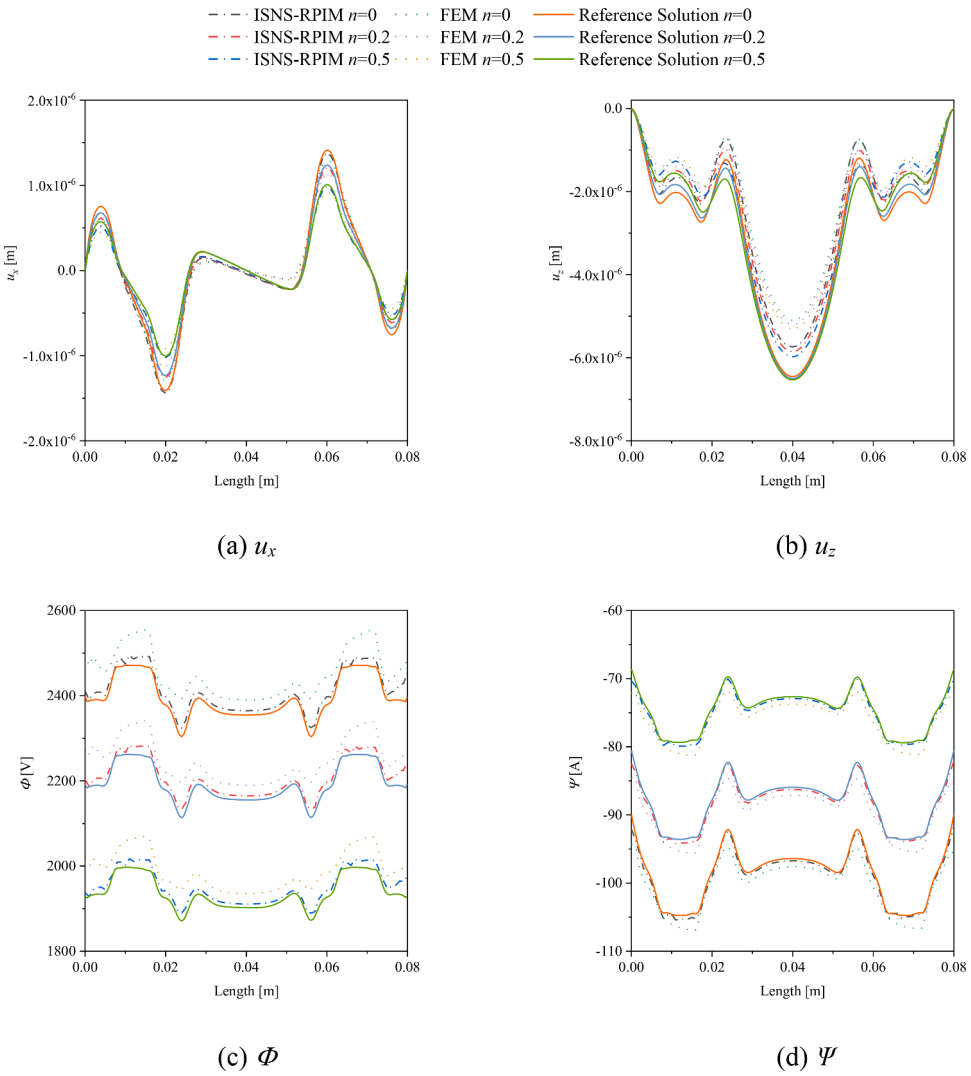

Fig. 15. The generalized displacement on edge AB ($\Delta T = 40$ K, $\Delta m = 3\%$).

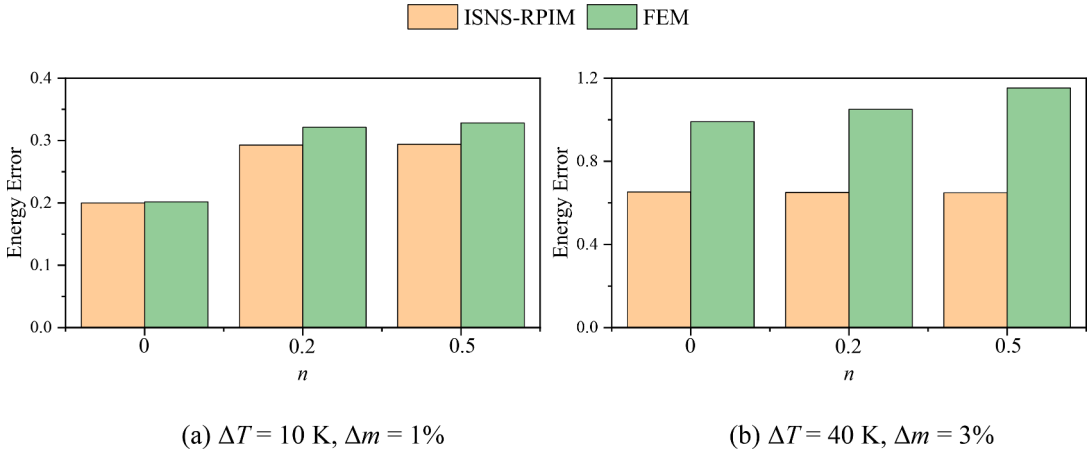

Fig. 16. The energy error of ISNS-RPIM and FEM.

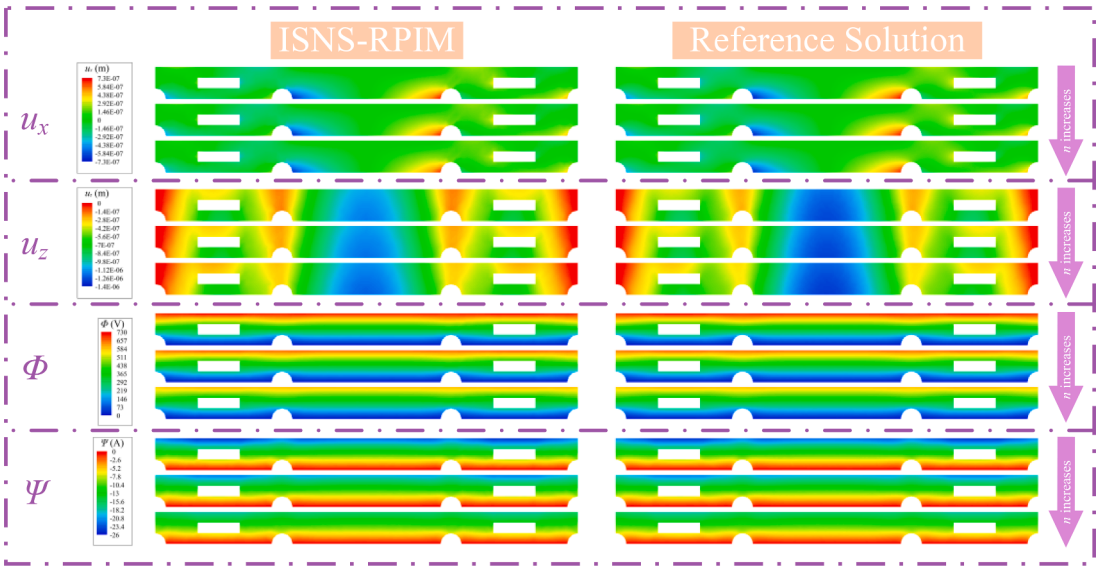

Fig. 17. Contours of the FGMEE sensor ($\Delta T = 10$ K, $\Delta m = 1\%$).

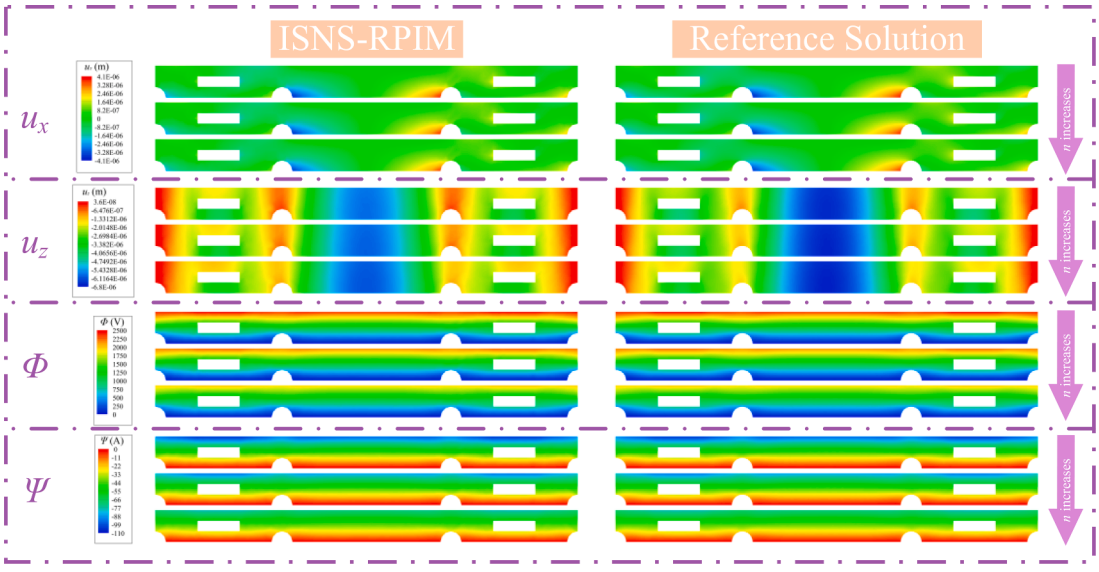

Fig. 18. Contours of the FGMEE sensor ($\Delta T = 40$ K, $\Delta m = 3\%$).

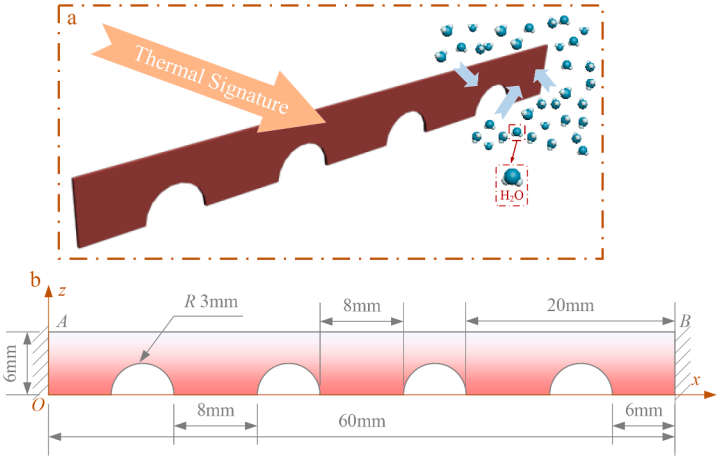

Fig. 19. (a) FGMEE energy harvester (b) Dimensions of the FGMEE energy harvester.

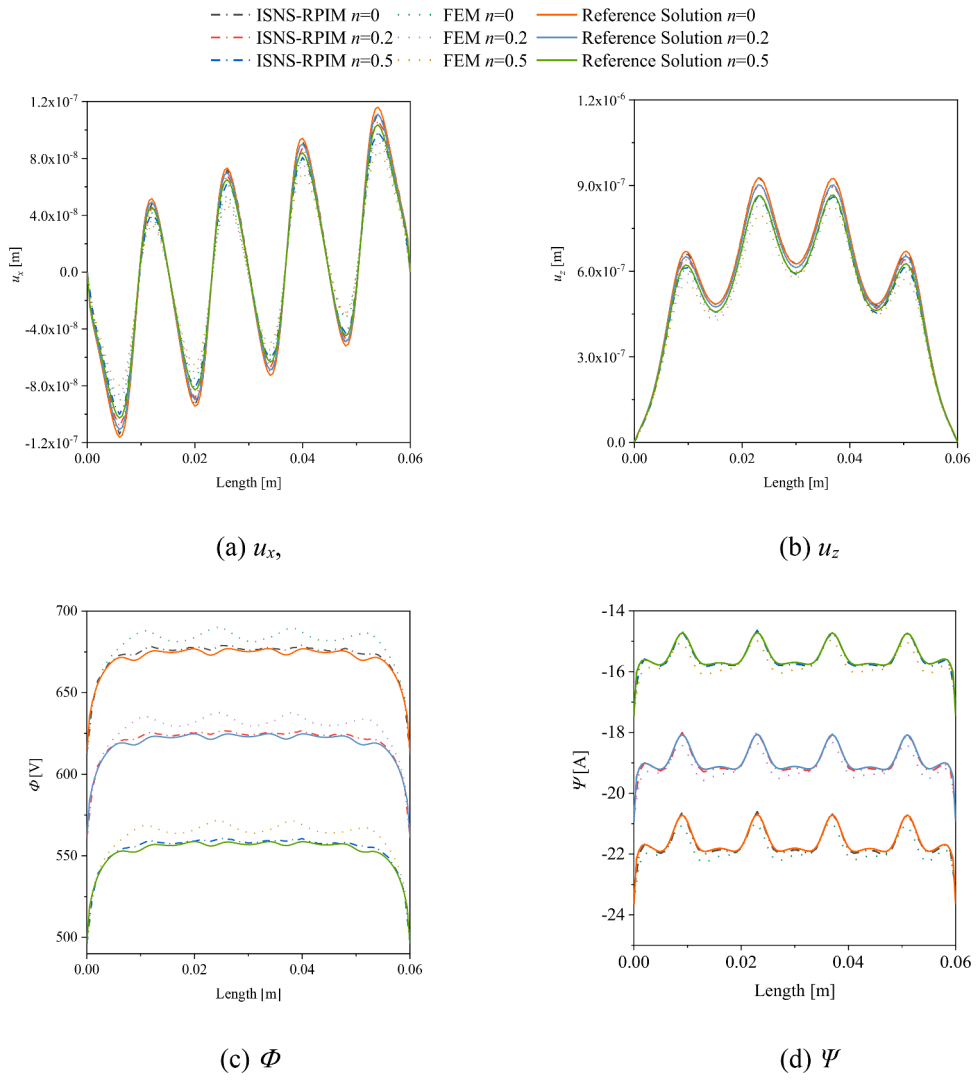

Fig. 20. The generalized displacement on edge AB ($\alpha^* = \beta^* = 0$).

dependent elastic stiffness coefficient $\widetilde{C}$ and the independent elastic stiffness coefficient C^* have the following relationship [28]

$$\widetilde{C} = C^* + C^*\alpha^*\Delta T + C^*\beta^*\Delta m \tag{72}$$

The error in total energy norm is introduced to verify the convergence and accuracy of ISNS-RPIM:

$$\text{EnergyError} = \sqrt{\frac{1}{2}\int\left(\begin{array}{l} C_{ijkl}\left(S_{ij}-S_{ij}^{\text{An}}\right)\left(S_{kl}-S_{kl}^{\text{An}}\right)+\varepsilon_{ij}\left(E_i-E_i^{\text{An}}\right)\left(E_j-E_j^{\text{An}}\right) \\ +\mu_{ij}\left(H_i-H_i^{\text{An}}\right)\left(H_j-H_j^{\text{An}}\right)\end{array}\right)d\Omega} \tag{73}$$

where the expressions of S_{ij}^{An}, E_i^{An} and H_i^{An} are given as

$$S_{ij}^{\text{An}} = \lim_{N\to\infty}\sum_{i=1}^{N}\left(\overline{B}_{\text{u}}^{i}\right)_{ijk}u_k, E_i^{\text{An}} = \lim_{N\to\infty}\sum_{i=1}^{N}\left(\overline{B}_{\Phi}^{i}\right)_{ij}\Phi, H_i^{\text{An}} = \lim_{N\to\infty}\sum_{i=1}^{N}\left(\overline{B}_{\Psi}^{i}\right)_{ij}\Psi \tag{74}$$

Demonstrate the efficiency of ISNS-RPIM through the parameter EC

$$EC = \frac{1}{\text{CPUtime}\times\text{EnergyError}} \tag{75}$$

Then, create the irregular meshes (x_{ir}, z_{ir}) as follow [56].

$$x_{ir} = x + r_{\text{A}}\cdot\Delta x\cdot\alpha_{ir} \tag{76}$$

$$z_{ir} = z + r_{\text{A}}\cdot\Delta z\cdot\alpha_{ir} \tag{77}$$

where α_{ir} represents the irregular factor whose value range is 0 to 0.5, r_{A} is the arbitrary number, Δx and Δz express the distances of regular nodes in the x-direction and z-direction.

The constraints corresponding to different boundary conditions are:
Free end: $u_x = u_z = \Phi = \Psi \neq 0$.

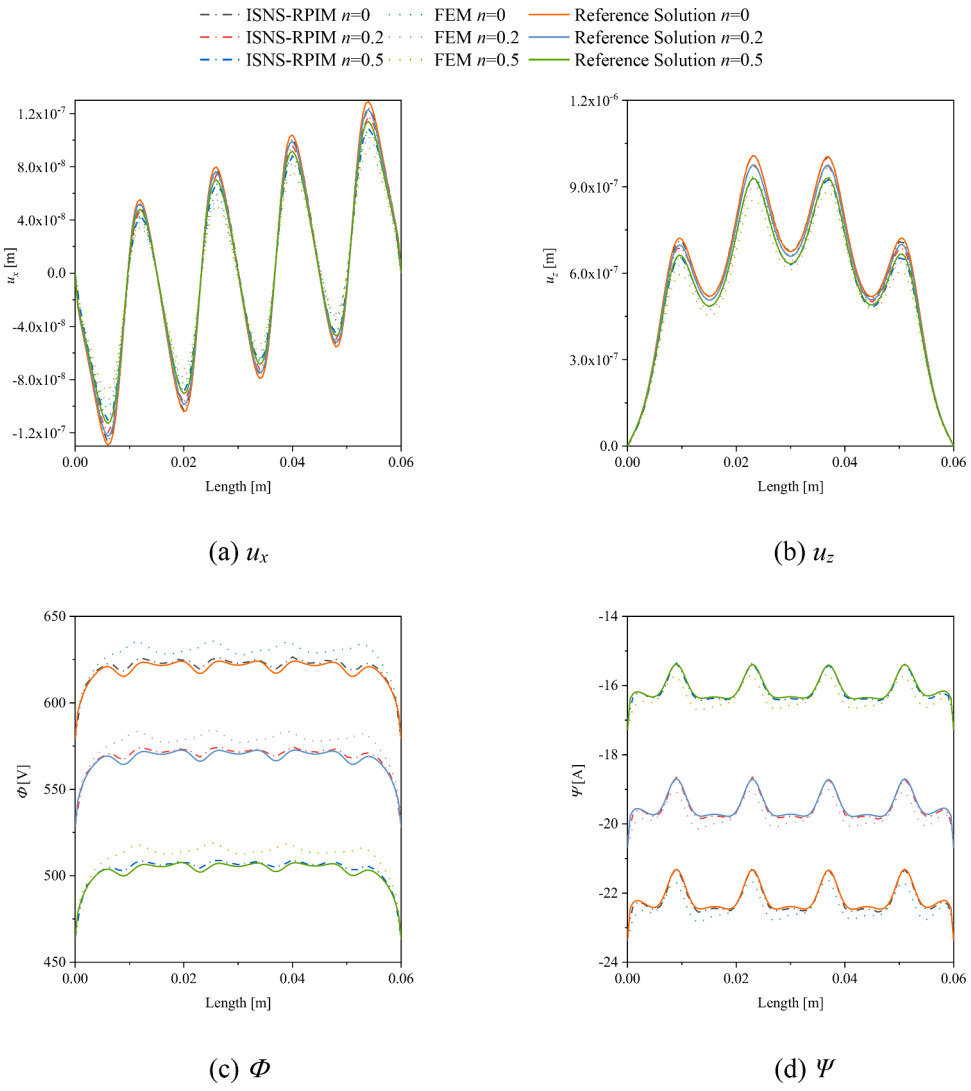

Fig. 21. The generalized displacement on edge AB ($\alpha^* = \beta^* = -0.05$).

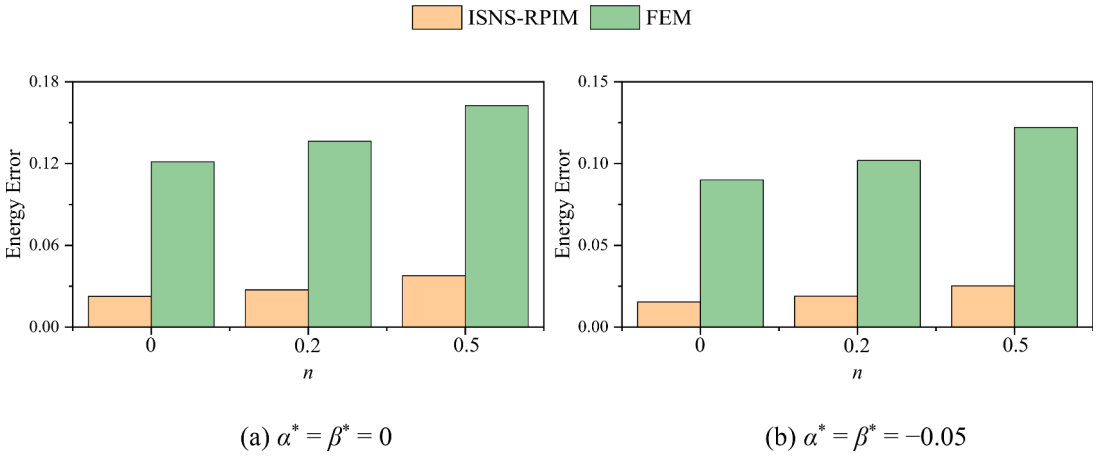

Fig. 22. Energy error.

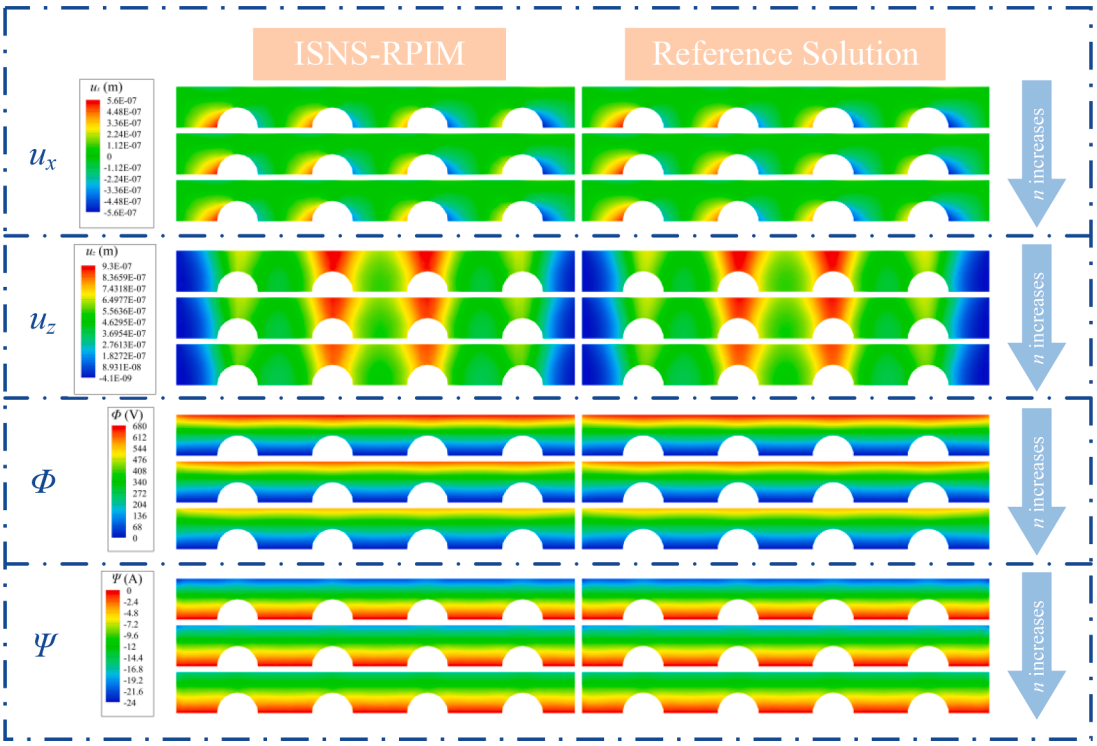

Fig. 23. FGMEE energy harvester Contours ($\alpha^* = \beta^* = 0$).

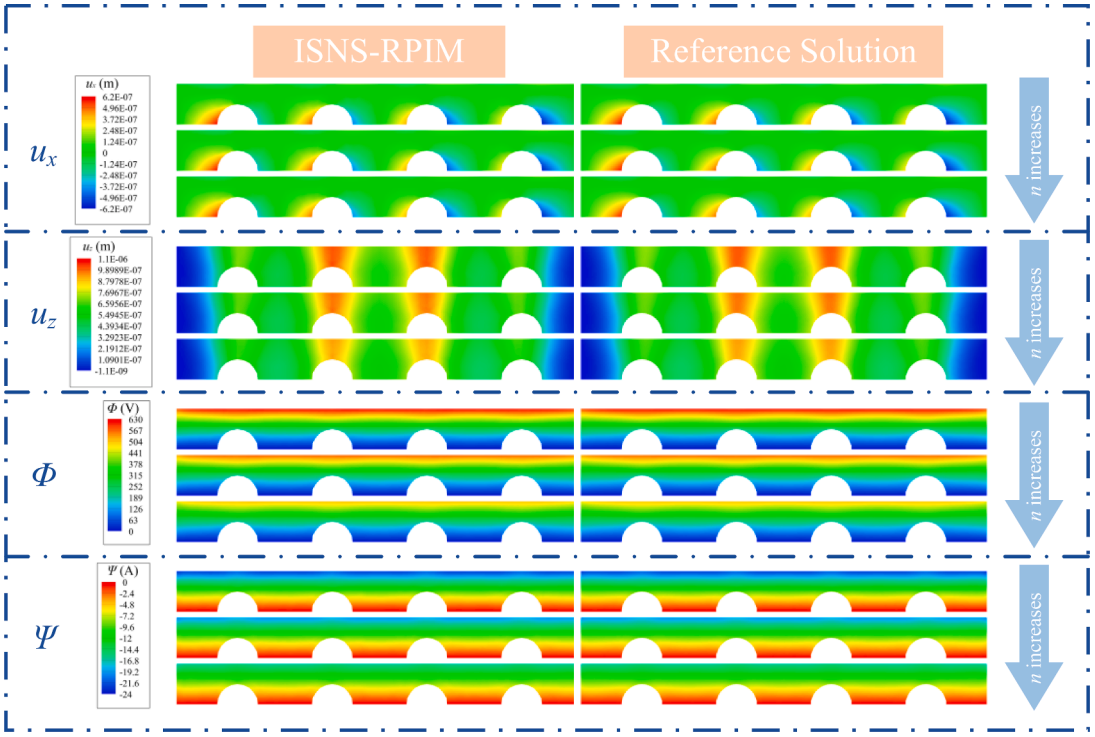

Fig. 24. FGMEE energy harvester contours ($\alpha^* = \beta^* = -0.05$).

Bottom edge: $\Phi = \Psi = 0$.
Clamped end: $u_x = u_z = 0$.

4.1. MEE plate

The developed method is used to study the generalized displacement for a $BaTiO_3$-$CoFe_2O_4$ in-plane plate to verify the correctness of ISNS-RPIM. Fig. 4 shows the meshes and dimensions of the structure subjected to a uniform load F (upward) at the upper edge, F= 100 N/m. The exponential factor is 0. The mechanical, electric and magnetic boundary conditions considered in the present work are:

$u_x = 0$ at z = -1 (AD)
$u_z = \Phi = \Psi = 0$ at x = -1 (CD)

Results at point B (1m, 1m) are given in Table 2. It can be observed that ISNS-RPIM displays a close agreement with the results of Zhu et al. [63]. Hence, ISNS-RPIM could produce sufficiently reliable results for

HMEE coupling problems. The formulation could be extended to analyze other structures with complex geometries, boundary conditions and loadings.

In the subsequent section, select the calculation results of FEM as the reference solution to further prove the advantages of ISNS-RPIM in solving HMEE coupling problems.

Table 3 shows the comparison of CPU time and error under different numerical methods. We compared the conclusion of ISNS-RPIM program with an existing reference solution element free Galerkin method (EFGM) [64]. It can be seen from Table 3 that the calculation efficiency of ISNS-RPIM is higher than FEM and EFGM, which proves the accuracy and high efficiency of ISNS-RPIM.

4.2. FGMEE beam

The static responses and free vibration for FGMEE clamped-clamped beam subject to hygrothermal loadings are researched in this section. The beam with length $L = 0.1$ m and width $W = 0.01$ m is shown in Fig. 5. The empirical constants are $\alpha^* = \beta^* = -0.01$.

4.2.1. Static and dynamic analysis for FGMEE beam

The exponential factor n is taken as 0, 0.2, 0.5. ISNS-RPIM uses triangular elements (427 nodes), and the calculation results as a reference using FEM based on quadrilateral elements (2737 nodes). Fig. 6 shows the generalized displacement on edge AB of the geometry, and Fig. 7 exhibits the contours of the whole mode. The variation of temperature and moisture are $\Delta T = 50$ K and $\Delta m = 1\%$, respectively. It can be observed that under the same hygrothermal loading and n, with the increase of n, values of u_x and Φ decrease and values of u_z and Ψ increases.

The same meshes are applied to solve the free vibration problem. Results are given in Fig. 8, the loadings are $\Delta T = 10$ K, $\Delta m = 1\%$ and $\Delta T = 20$ K, $\Delta m = 2\%$ and $\Delta T = 50$ K, $\Delta m = 3\%$, the exponential factors are $n = 0$, 0.2, 0.5. It is obvious that, because of the existence of empirical constants affects the elastic stiffness coefficient, the natural frequency of the model decreases when the loading gradually increases. Where α^* and β^* are negative, the elastic stiffness coefficient and the model stiffness decrease due to the increase in ΔT and Δm. Fig. 9 shows the relative error values of the free vibration problem between different algorithms and reference solutions. The relative error of ISNS-RPIM is smaller than other algorithms including NS-RPIM and FEM. In addition, the figures reveal that NS-RPIM is inaccurate in solving the free vibration problem due to the temporal instability, which is far from the reference solution. Therefore, ISNS-RPIM has extremely high accuracy when solving statics and free vibration problems of FGMEE structures.

4.2.2. Energy error and efficiency study

The energy error, CPU time and efficiency are shown in Fig. 10 with different algorithms including ISNS-RPIM, NS-RPIM and FEM. $\Delta T = 10$ K, $\Delta m = 1\%$ and $\Delta T = 20$ K, $\Delta m = 2\%$ are the hygrothermal loadings, $n = 0$, 0.2, 0.5 are the exponential factors. 63, 205, 427 and 729 nodes were used for calculation. The expression of h is $h = \sqrt{4\overline{A}/\sqrt{3}}$, which represents the characteristic length. $\overline{A}$ is the mean size of the element. The smaller the h, the more nodes are required for the computation. It is evident that the error decreases as h decreases, which illustrates the convergence of ISNS-RPIM. The errors of ISNS-RPIM are the smallest under any loadings and exponential factor. In terms of CPU time, NS-RPIM has longer calculation time than FEM due to the smoothing operation. ISNS-RPIM is based on NS-RPIM, and it also needs to calculate the stable terms, thus ISNS-RPIM takes the longest time to calculate the same problem.

EC is an indicator describing the efficiency of the algorithm. ISNS-RPIM with 63 nodes is not the most efficient one. However, in other cases, ISNS-RPIM has higher efficiency. In process of solving practical engineering problems, the requirements for accuracy and efficiency are very high. ISNS-RPIM could combine high accuracy with high efficiency. Therefore, ISNS-RPIM is an algorithm suitable for solving practical HMEE coupling problems.

4.2.3. Mesh distortion effect

The influence of irregular factor α_{ir} on ISNS-RPIM is researched. Ten irregular factors are considered, $\alpha_{ir} = 0.05$, 0.1, 0.15, 0.2, 0.25, 0.3, 0.35, 0.4, 0.45, 0.5, the larger the α_{ir}, the more irregular the meshes. Run the process ten times to obtain ten sets of generalized displacement. Then take the average of these ten groups of results and draw the curves on edge AB (Fig. 11) and calculate the errors (Fig. 12). A total of 245 nodes are used for calculation, two sets of hygrothermal loadings are considered, $\Delta T = 10$ K, $\Delta m = 1\%$ and $\Delta T = 20$ K, $\Delta m = 2\%$. When $\alpha_{ir} > 0.3$, Jacobian matrix could obtain negative determination, which reduces the accuracy of FEM [46]. It can be seen from the results that ISNS-RPIM is the algorithm with the best agreement with the reference solution, which possesses the lowest error. There are no Jacobian matrix and coordinate transformation needed in the calculation process of ISNS-RPIM, thus, the ISNS-RPIM is insensitive to distorted mesh.

4.3. Static responses of FGMEE sensor using ISNS-RPIM

After verifying the superiority of ISNS-RPIM, the HMEE coupling problems of complex FGMEE structures are analyzed, empirical constants and exponential factor are also taken into consideration to explore the impact on the results.

4.3.1. Influence of ΔT and Δm

In Fig. 13, consider a FGMEE sensor with fully clamped on left and right sides. ISNS-RPIM and FEM use triangular elements (570 nodes), and the reference solution uses quadrilateral meshes with a much denser mesh (2060 nodes). In this section, two hygrothermal loadings are considered: $\Delta T = 10$ K, $\Delta m = 1\%$ and $\Delta T = 40$ K, $\Delta m = 3\%$. The empirical constants are $\alpha^* = \beta^* = -0.02$, Consider the case where the exponential factor n is 0, 0.2, 0.5.

Figs. 14 and 15 display the u_x, u_z, Φ, Ψ on edge AB, Fig. 16. exhibits the energy errors. The contours of the FGMEE sensor under different hygrothermal loadings and exponential factors are shown in Figs. 17 and 18. It can be seen that when the values of α^*, β^* and n remain unchanged, the increases in ΔT and Δm result in the increase of the generalized displacement. ΔT and Δm increase, the structural stiffness decreases. In addition, Φ and Ψ are greatly affected by n. As n increases, the absolute values of u_x, Φ and Ψ decrease, those of u_z increases. According to Eq. (5), it can be seen that when $n > 0$, the stiffness of the structure increases, when the hygrothermal loading is kept constant, the displacement decreases. The form of the structure has an effect on the local displacement. The form of the structure has an effect on the local displacement.

It is clear that ISNS-RPIM is the most accurate one, whose results fit well with reference solutions, which proves again the correctness of ISNS-RPIM.

4.3.2. Effective of empirical constants α^* and β^*

Next, we consider a FGMEE energy harvester with four semicircular holes at the bottom edge, left and right edges are both clamped in Fig. 19. In this section, $\Delta T = 10$ K, $\Delta m = 1\%$. $\alpha^* = \beta^* = 0$ and $\alpha^* = \beta^* = -0.05$ are the empirical constants, $n = 0$, 0.2, 0.5 are the exponential factor. ISNS-RPIM and FEM use triangular elements (416 nodes), the results as a reference based on quadrilateral meshes with a much denser mesh (1476 nodes).

Figs. 20 and 21 exhibit the generalized displacement on edge AB. Fig. 22 is the energy error of two algorithms. The contours of the FGMEE energy harvester are given in Figs. 23 and 24. When ΔT, Δm and n do not change, the decrease of empirical constants leads to the decrease of structural stiffness. Therefore, values of u_x and u_z both increase, which is consistent with Eq. (50). Meanwhile, Φ and Ψ decrease. It can also be

seen that Φ and Ψ are greatly affected by n. As n increases, the value of Φ decreases and the value of Ψ increases. The displacement is less affected by n, which decreases as n increases.

It is obvious that the error of ISNS-RPIM is the lowest, indicating that the developed method is feasible and valid in tackling complex FGMEE structures in hygrothermal environment.

5. Conclusion

The ISNS-RPIM is presented to explore FGMEE structures. The stable terms related to field variables are employed to improve the temporal stability of NS-RPIM. The factors influencing structural static responses and natural frequency are investigated in detail: exponential factor and hygrothermal loadings. Results show that increasing the empirical constants decreased the structural stiffness and the natural frequency. For exponential factors, u_x, Φ decrease and Ψ increases, as the exponential factor increase. In addition, Φ and Ψ are greatly affected by the exponential factor. Finally, the results also show the advantages of high precision, high effectiveness, and insensitivity to mesh distortion in ISNS-RPIM, which verifies the robustness of ISNS-RPIM and shows the potential of the algorithm in solving practical complex problems. (Eqs. (1)–(4), (8), (10)–(12), (17)–(21), (23), (25)–(48), (52)–(77))

Declaration of Competing Interest

The authors declare that they have no conflicts of interest.

Data availability

No data was used for the research described in the article.

Acknowledgments

This work was supported by the National Natural Science Foundation of China (Grant Number. 51975243); Project of Science and Technology Department of Jilin Province (Grant Number. 20210101405JC) and Interdisciplinary Cultivation Project for Young Teachers and Students of Jilin University (Grant Number. 2020-JCXK-08). The financial support by The Royal Society, London through Newton International Fellowship (NIF\R1\212432) is sincerely acknowledged by the author Vinyas Mahesh.

References

[1] Saadatfar M. Multiphysical time-dependent creep response of FGMEE hollow cylinder in thermal and humid environment. Mech Time Depend Mater 2019;25(2):151–73. https://doi.org/10.1007/s11043-019-09433-0.
[2] Zhang PC, Qi CZ, Fang HY, Sun X. A semi-analytical approach for the flexural analysis of in-plane functionally graded magneto-electro-elastic plates. Compos Struct 2020;250:112590. https://doi.org/10.1016/j.compstruct.2020.112590.
[3] Shariati A, Jung DW, Mohammad-Sedighi H, Zur KK, Habibi M, Safa M. On the Vibrations and Stability of Moving Viscoelastic Axially Functionally Graded Nanobeams. Materials 2020;13(7):1707. https://doi.org/10.3390/ma13071707.
[4] Zur KK, Arefi M, Kim J, Reddy JN. Free vibration and buckling analyses of magneto-electro-elastic FGM nanoplates based on nonlocal modified higher-order sinusoidal shear deformation theory. Compos Part B Eng 2020;182:107601. https://doi.org/10.1016/j.compositesb.2019.107601.
[5] Dai T, Dai HL, Lin ZY. Multi-field mechanical behavior of a rotating porous FGMEE circular disk with variable thickness under hygrothermal environment. Compos Struct 2019;210:641–56. https://doi.org/10.1016/j.compstruct.2018.11.077.
[6] Nan CW. Magnetoelectric effect in composites of piezoelectric and piezomagnetic phases. Phys Rev B 1994;50(9):6082–8. https://doi.org/10.1103/PhysRevB.50.6082.
[7] Benveniste Y. Magnetoelectric effect in fibrous composites with piezoelectric and piezomagnetic phases. Phys Rev B 1995;51(22):16424–7. https://doi.org/10.1103/PhysRevB.51.16424.
[8] Shishesaz M, Shirbani MM, Sedighi HM, Hajnayeb A. Design and analytical modeling of magneto-electromechanical characteristics of a novel magneto-electro-elastic vibration-based energy harvesting system. J Sound Vib 2018;425:149–69. https://doi.org/10.1016/j.jsv.2018.03.030.
[9] Shirbani MM, Shishesaz M, Sedighi HM, Hajnayeb A. Parametric modeling of a novel longitudinal vibration-based energy harvester using magneto-electro-elastic materials. Microsyst Technol 2017;23(12):5989–6004. https://doi.org/10.1007/s00542-017-3402-0.
[10] Ansari R, Gholami R, Rouhi H. Geometrically nonlinear free vibration analysis of shear deformable magneto-electro-elastic plates considering thermal effects based on a novel variational approach. Thin Wall Struct 2019;135:12–20. https://doi.org/10.1016/j.tws.2018.10.033.
[11] Thai H-T, Kim S-E. A review of theories for the modeling and analysis of functionally graded plates and shells. Compos Struct 2015;128:70–86. https://doi.org/10.1016/j.compstruct.2015.03.010.
[12] Chen JY, Guo JH, Pan EN. Reflection and transmission of plane wave in multilayered nonlocal magneto-electro-elastic plates immersed in liquid. Compos Struct 2017;162:401–10. https://doi.org/10.1016/j.compstruct.2016.11.004.
[13] Pan E, Waksmanski N. Deformation of a layered magnetoelectroelastic simply-supported plate with nonlocal effect, an analytical three-dimensional solution. Smart Mater Struct 2016;25(9):095013. https://doi.org/10.1088/0964-1726/25/9/095013.
[14] Pan E. Three-dimensional Green's functions in anisotropic magneto-electro-elastic bimaterials. Z Angew Math Phys ZAMP 2002;53(5):815–38. https://doi.org/10.1007/s00033-002-8184-1.
[15] Hughes TJR. The Finite Element Method: Linear Static and Dynamic Finite Element Analysis. New Jersey: Prentice-Hall; 1987.
[16] Liu GR, Quek SS. The Finite Element Method: A Practical Course. Oxford: Butterworth-Heinemann; 2013.
[17] Bhangale RK, Ganesan N. Static analysis of simply supported functionally graded and layered magneto-electro-elastic plates. Int J Solids Struct 2006;43(10):3230–53. https://doi.org/10.1016/j.ijsolstr.2005.05.030.
[18] Bhangale RK, Ganesan N. Free vibration of simply supported functionally graded and layered magneto-electro-elastic plates by finite element method. J Sound Vib 2006;294(4-5):1016–38. https://doi.org/10.1016/j.jsv.2005.12.030.
[19] Abbas IA, Zenkour AM. LS model on electro-magneto-thermoelastic response of an infinite functionally graded cylinder. Compos Struct 2013;96:89–96. https://doi.org/10.1016/j.compstruct.2012.08.046.
[20] Zenkour AM, Abbas IA. Magneto-thermoelastic response of an infinite functionally graded cylinder using the finite element method. J Vib Control 2014;20(12):1907–19. https://doi.org/10.1177/1077546313480541.
[21] Zenkour AM, Abbas IA. Electro-magneto-thermo-elastic response of infinite functionally graded cylinders without energy dissipation. J Magn Magn Mater 2015;395:123–9. https://doi.org/10.1016/j.jmmm.2015.07.038.
[22] Kattimani SC, Ray MC. Control of geometrically nonlinear vibrations of functionally graded magneto-electro-elastic plates. Int J Mech Sci 2015;99:154–67. https://doi.org/10.1016/j.ijmecsci.2015.05.012.
[23] Kiran MC, Kattimani SC. Assessment of porosity influence on vibration and static behaviour of functionally graded magneto-electro-elastic plate: a finite element study. Eur J Mech a-Solid 2018;71:258–77. https://doi.org/10.1016/j.euromechsol.2018.04.006.
[24] Ebrahimi F, Barati MR. Wave propagation analysis of smart strain gradient piezo-magneto-elastic nonlocal beams. Struct Eng Mech 2018;66(2):237–48. https://doi.org/10.12989/sem.2018.66.2.237.
[25] Mahesh V, Sagar PJ, Kattimani S. Influence of coupled fields on free vibration and static behavior of functionally graded magneto-electro-thermo-elastic plate. J Intell Mater Syst 2018;29(7):1430–55. https://doi.org/10.1177/1045389X17740739.
[26] Mahesh V, Harursampath D. Nonlinear vibration of functionally graded magneto-electro-elastic higher order plates reinforced by CNTs using FEM. Eng Comput 2020;38(2):1029–51. https://doi.org/10.1007/s00366-020-01098-5.
[27] Vinyas M. On frequency response of porous functionally graded magneto-electro-elastic circular and annular plates with different electro-magnetic conditions using HSDT. Compos Struct 2020;240:112044. https://doi.org/10.1016/j.compstruct.2020.112044.
[28] Vinyas M, Kattimani SC, Joladarashi S. Hygrothermal coupling analysis of magneto-electroelastic beams using finite element methods. J Therm Stresses 2018;41(8):1063–79. https://doi.org/10.1080/01495739.2018.1447856.
[29] Vinyas M, Kattimani SC. Hygrothermal analysis of magneto-electro-elastic plate using 3D finite element analysis. Compos Struct 2017;180:617–37. https://doi.org/10.1016/j.compstruct.2017.08.015.
[30] Vinyas M, Kattimani SC. Finite element evaluation of free vibration characteristics of magnetoelectro-elastic rectangular plates in hygrothermal environment using higher-order shear deformation theory. Compos Struct 2018;202:1339–52. https://doi.org/10.1016/j.compstruct.2018.06.069.
[31] Vinyas M, Harursampath D. Computational evaluation of electro-magnetic circuits' effect on the coupled response of multifunctional magneto-electro-elastic composites plates exposed to hygrothermal fields. Proc Inst Mech Eng Part C J Mech Eng Sci 2020;235(15):2832–50. https://doi.org/10.1177/0954406220954485.
[32] Mahesh V, Kattimani S, Harursampath D, Trung NT. Coupled evaluation of the free vibration characteristics of magneto-electro-elastic skew plates in hygrothermal environment. Smart Struct Syst 2019;24(2):267–92. https://doi.org/10.12989/sss.2019.24.2.267.
[33] Jafari E, Fakoor M, Karvand E. Hygrothermal free vibration of multiple magneto-electro-elastic nanoplate system via higher-order nonlocal strain gradient theory. Appl Phys Part A Mater 2019;125(9):607. https://doi.org/10.1007/s00339-019-2855-7.
[34] Nguyen-Thoi T, Ly KD, Truong TT, Nguyen SN, Mahesh V. Analysis and optimal control of smart damping for porous functionally graded magneto-electro-elastic

plate using smoothed FEM and metaheuristic algorithm. Eng Struct 2022;259:114062. https://doi.org/10.1016/j.engstruct.2022.114062.
[35] Liu GR, Nguyen TT, Dai KY, Lam KY. Theoretical aspects of the smoothed finite element method (SFEM). Int J Numer Methods Eng 2007;71(8):902–30. https://doi.org/10.1002/nme.1968.
[36] Cao X, Cai Y, Cui X. A parallel numerical acoustic simulation on a GPU using an edge-based smoothed finite element method. Adv Eng Softw 2020;148:102835. https://doi.org/10.1016/j.advengsoft.2020.102835.
[37] Wu F, Yao LY, Hu M, He ZC. A stochastic perturbation edge-based smoothed finite element method for the analysis of uncertain structural-acoustics problems with random variables. Eng Anal Bound Elem 2017;80:116–26. https://doi.org/10.1016/j.enganabound.2017.03.008.
[38] Tang BX, Li S, Cui XY. A gradient weighted finite element method (GW-FEM) for static and quasi-static electromagnetic field computation. Int J Comput Methods 2020;17(6):1950017. https://doi.org/10.1142/S0219876219500178.
[39] Liu GR, Zhang GY. Smoothed point interpolation method: G space theory and weakened weak forms. World Scientific; 2013.
[40] Liu GR. On G space theory. Int J Comput Methods 2009;6(2):257–89. https://doi.org/10.1142/S0219876209001863.
[41] Khoshghalb A, Shafee A, Tootoonchi A, Ghaffaripour O, Jazaeri SA. Application of the smoothed point interpolation methods in computational geomechanics: a comparative study. Comput Geotech 2020;126:103714. https://doi.org/10.1016/j.compgeo.2020.103714.
[42] Zhang GY, Liu GR, Nguyen TT, Song CX, Han X, Zhong ZH, et al. The upper bound property for solid mechanics of the linearly conforming radial point interpolation method (LC-RPIM). Int J Comput Methods 2007;4(3):521–41. https://doi.org/10.1142/S0219876207001308.
[43] Liu GR, Li Y, Dai KY, Luan MT, Xue W. A linearly conforming radial point interpolation method for solid mechanics problems. Int J Comput Methods 2006;3(4):401–28. https://doi.org/10.1142/S0219876206001132.
[44] Zhou L, Ren S, Meng G, Ma Z. Node-based smoothed radial point interpolation method for electromagnetic-thermal coupled analysis. Appl Math Model 2020;78:841–62. https://doi.org/10.1016/j.apm.2019.09.047.
[45] Li Y, Liu GR, Yue JH. A novel node-based smoothed radial point interpolation method for 2D and 3D solid mechanics problems. Comput Struct 2018;196:157–72. https://doi.org/10.1016/j.compstruc.2017.11.010.
[46] Li Y, Liu G, Feng Z, Ng K, Li S. A node-based smoothed radial point interpolation method with linear strain fields for vibration analysis of solids. Eng Anal Bound Elem 2020;114:8–22. https://doi.org/10.1016/j.enganabound.2020.01.018.
[47] Zhang GY, Li Y, Gao XX, Hui D, Wang SQ, Zong Z. Smoothed point interpolation method for elastoplastic analysis. Int J Comput Methods 2015;12(4):1540013. https://doi.org/10.1142/S0219876215400137.
[48] Zhang ZQ, Liu GR. Temporal stabilization of the node-based smoothed finite element method and solution bound of linear elastostatics and vibration problems. Comput Mech 2010;46(2):229–46. https://doi.org/10.1007/s00466-009-0420-5.
[49] Zhao JW, Feng SZ, Tao YR, Li ZX. Stable node-based smoothed extended finite element method for fracture analysis of structures. Comput Struct 2020;240:106357. https://doi.org/10.1016/j.compstruc.2020.106357.
[50] He ZC, Liu GR, Zhong ZH, Zhang GY, Cheng AG. Dispersion free analysis of acoustic problems using the alpha finite element method. Comput Mech 2010;46(6):867–81. https://doi.org/10.1007/s00466-010-0516-y.
[51] Wang G, Cui XY, Feng H, Li GY. A stable node-based smoothed finite element method for acoustic problems. Comput Methods Appl Mech ;297:348–70. https://doi.org/10.1016/j.cma.2015.09.005.
[52] Ren S, Meng G, Nie B, Zhou L, Zhao H. A novel stabilized node-based smoothed radial point interpolation method (SNS-RPIM) for coupling analysis of magneto-electro-elastic structures in hygrothermal environment. Comput Methods Appl Mech 2020;365:112975. https://doi.org/10.1016/j.cma.2020.112975.
[53] Chen L, Zhang YW, Liu GR, Nguyen-Xuan H, Zhang ZQ. A stabilized finite element method for certified solution with bounds in static and frequency analyses of piezoelectric structures. Comput Methods Appl Mech 2012;241-244:65–81. https://doi.org/10.1016/j.cma.2012.05.018.
[54] Feng H, Cui XY, Li GY, Feng SZ. A temporal stable node-based smoothed finite element method for three-dimensional elasticity problems. Comput Mech 2014;53(5):859–76. https://doi.org/10.1007/s00466-013-0936-6.
[55] Liu GR, Nguyen-Thoi T, Lam KY. A novel alpha finite element method (alpha FEM) for exact solution to mechanics problems using triangular and tetrahedral elements. Comput Methods Appl Mech 2008;197(45-48):3883–97. https://doi.org/10.1016/j.cma.2008.03.011.
[56] Ren S, Meng G, Wang J, Zhou L, Zhao H. A stabilized node-based smoothed radial point interpolation method for functionally graded magneto-electro-elastic structures in thermal environment. Compos Struct 2020;234:111674. https://doi.org/10.1016/j.compstruct.2019.111674.
[57] Ye W, Liu J, Zang Q, Lin G. Magneto-electro-elastic semi-analytical models for free vibration and transient dynamic responses of composite cylindrical shell structures. Mech Mater 2020;148:103495. https://doi.org/10.1016/j.mechmat.2020.103495.
[58] You X, Chai Y, Li W. A coupled FE-meshfree method for Helmholtz problems using point interpolation shape functions and edge-based gradient smoothing technique. Comput Struct 2019;213:1–22. https://doi.org/10.1016/j.compstruc.2018.07.011.
[59] Zhang GY, Chen ZC, Sui ZX, Tao DS, He ZC, Tang Q, et al. A cell-based smoothed radial point interpolation method with virtual nodes for three-dimensional mid-frequency acoustic problems. Int J Numer Methods Eng 2019;119(6):548–66. https://doi.org/10.1002/nme.6062.
[60] Liu GR, Gu YT. An introduction to meshfree methods and their programming. Springer; 2005.
[61] Wang JG, Liu GR. A point interpolation meshless method based on radial basis functions. Int J Numer Methods Eng 2002;54(11):1623–48. https://doi.org/10.1002/nme.489.
[62] Liu GR, Zhang GY. Upper bound solution to elasticity problems: a unique property of the linearly conforming point interpolation method (LC-PIM). Int J Numer Methods Eng 2008;74(7):1128–61. https://doi.org/10.1002/nme.2204.
[63] Zhu XY, Huang ZY, Jiang AM, Chen WQ, Nishimura N. Fast multipole boundary element analysis for 2D problems of magneto-electro-elastic media. Eng Anal Bound Elem 2010;34(11):927–33. https://doi.org/10.1016/j.enganabound.2010.06.006.
[64] Zhou LM, Wang JY, Li XL, Chen WQ, Liu P, Ren SH, Li M. The magneto-electro-elastic multi-physics coupling element free Galerkin method for smart structures in statics and dynamics problems. Thin Wall Struct 2021;169:108431. https://doi.org/10.1016/j.tws.2021.108431.